

LA-UR-23-27371

Accepted Manuscript

Plasma pressure distribution of ions and electrons in the inner magnetosphere during CIR driven storms observed during Arase era

Kumar, Sandeep; Miyoshi, Yoshizumi; Jordanova, Vania Koleva; Kistler, L. M.; Park, I.; Jun, C.; Hori, T.; Asamura, K.; Shreedevi, P. R.; Yokota, S.; Kasahara, S.; Kazama, Y.; Wang, S.-Y.; Tam, Sunny; Chang, T. F.; Mitani, T.; Higashio, N.; Keika, K.; Matsuoka, A.; Imajo, S.; Shinohara, I.; et al.

Provided by the author(s) and the Los Alamos National Laboratory (2023-09-08).

To be published in: Journal of Geophysical Research: Space Physics

DOI to publisher's version: 10.1029/2023JA031756

Permalink to record:

<https://permalink.lanl.gov/object/view?what=info:lanl-repo/lareport/LA-UR-23-27371>



Los Alamos National Laboratory, an affirmative action/equal opportunity employer, is operated by Triad National Security, LLC for the National Nuclear Security Administration of U.S. Department of Energy under contract 89233218CNA000001. By approving this article, the publisher recognizes that the U.S. Government retains nonexclusive, royalty-free license to publish or reproduce the published form of this contribution, or to allow others to do so, for U.S. Government purposes. Los Alamos National Laboratory requests that the publisher identify this article as work performed under the auspices of the U.S. Department of Energy. Los Alamos National Laboratory strongly supports academic freedom and a researcher's right to publish; as an institution, however, the Laboratory does not endorse the viewpoint of a publication or guarantee its technical correctness.

Plasma pressure distribution of ions and electrons in the inner magnetosphere during CIR driven storms observed during Arase era

Sandeep Kumar¹, Y. Miyoshi¹, V. Jordanova², L. M. Kistler^{1,3}, I. Park¹, C. Jun¹, T. Hori¹, K. Asamura⁴, Shreedevi P. R¹, S. Yokota⁵, S. Kasahara⁶, Y. Kazama⁷, S.-Y. Wang⁷, Sunny W. Y. Tam⁸, Tzu-Fang Chang⁸, T. Mitani⁴, N. Higashio⁴, K. Keika⁶, A. Matsuoka⁹, S. Imajo⁸, I. Shinohara⁴

¹ Institute for Space-Earth Environmental Research, Nagoya University, Nagoya, Japan

² Space Science and Application, Los Alamos National Laboratory, Los Alamos, NM, USA

³ University of New Hampshire, Durham, NH, USA,

⁴ ISAS/JAXA, Sagami-hara, Japan,

⁵ Osaka University, Suita, Japan

⁶ University of Tokyo, Tokyo, Japan,

⁷ ASIAA, Taipei, Taiwan,

⁸ Institute of Space and Plasma Sciences, National Cheng Kung University, Taiwan

⁹ Kyoto University, Kyoto, Japan

Corresponding author: Sandeep Kumar (sandeepk.iig@gmail.com)

Key Points:

- ✓ The first statistical study of both ring current ions (H^+ , He^+ , O^+) and electrons during CIR driven storms using Arase observations
- ✓ H^+ is the major contributor to the total pressure with $E=20-50$ keV while O^+ pressure with $E=10-20$ keV contributed more during main phase
- ✓ Electron ($E < 50$ keV) contributes $\sim 20\%$ to the total ring current pressure in 03-09 MLT during main and early recovery phase

This article has been accepted for publication and undergone full peer review but has not been through the copyediting, typesetting, pagination and proofreading process, which may lead to differences between this version and the [Version of Record](#). Please cite this article as [doi: 10.1029/2023JA031756](https://doi.org/10.1029/2023JA031756).

This article is protected by copyright. All rights reserved.

Abstract

Using Arase observations of the inner magnetosphere during 26 CIR-driven geomagnetic storms with minimum Sym-H between -33 and -86 nT, we investigated ring current pressure development of ions (H^+ , He^+ , O^+) and electron during prestorm, main, early recovery and late recovery phases as a function of L-shell and magnetic local time. It is found that during the main and early recovery phase of the storms the ion pressure is asymmetric in the inner magnetosphere, leading to a strong partial ring current. The ion pressure becomes symmetric during the late recovery phase. H^+ ions with energies of ~20-50 keV and ~50-100 keV contribute more to the ring current pressure during the main phase and early/late recovery phase, respectively. O^+ ions with energies of ~10-20 keV contribute significantly during main and early recovery phase. These are consistent with previous studies. The electron pressure was found to be asymmetric during the main, early recovery and late recovery phase. The electron pressure peaks from midnight to the dawn sector. Electrons with energy of <50 keV contribute to the ring current pressure during the main and early recovery phase of the storms. Overall, the electron contribution to the total ring current is found to be ~11% during the main and early recovery phases. However, the electron contribution is found to be significant (~22%) in the 03-09 MLT sector during the main and early recovery phase. The results indicate an important role of electrons in the ring current build up.

1. Introduction

Geomagnetic storms are the magnetic disturbances in the Earth's magnetic field and cause different space weather effects on the Earth. Interplanetary coronal mass ejections (ICMEs) and corotating interaction regions (CIRs) are the most common solar wind drivers of geomagnetic storms (Gonzalez et al., 1994, Echer et al., 2013). ICMEs are transient events with large clouds of plasma and magnetic fields ejected from the solar atmosphere (Burlaga et al., 1981; Klein and Burlaga, 1982; Cane and Richardson, 2003). CIRs are the results of high-speed solar wind streams (HSS) emanating from coronal holes interacting with ambient slow streams (Gosling and Pizzo, 1999; Alves et al., 2006; Tsurutani et al., 2006 and references therein). It is well known that ICME-driven and CIR-driven storms have different evolutions of the Dst index and the ion distributions in the inner magnetosphere (Miyoshi and Kataoka, 2005). It has been reported that the intense storms are mostly caused by the CMEs (Gonzalez et al., 1999; Miyoshi and Kataoka, 2011). The CIR-driven storms are generally weaker than CME-driven storms and no super intense storms are driven by CIRs (Borovsky and Denton, 2006; Echer et al., 2013; Tsurutani et al., 2006). It has been found that during CIR driven

This article is protected by copyright. All rights reserved.

storms, there is effective flux enhancement of relativistic electrons at geosynchronous orbit (Dmitriev et al., 2005, Miyoshi and Kataoka, 2005, 2008). However, during CME-driven storms the effective flux enhancements of the radiation belts can be seen at lower L shells ($L < 3$) (Miyoshi and Kataoka, 2005).

During geomagnetic storms, the coupling of the solar wind with the Earth's magnetosphere allows the energy transfer from the solar wind to the Earth's magnetosphere (Dungey, 1961). The enhancement of the ring current is one manifestation of this coupling (Daglis et al., 1999). Singer (1957) was first to suggest the existence of the westward equatorial ring current around the Earth at 2–9 R_E . The ring current is composed of charged particles with energies of few kilo electron volts (keVs) to a few hundreds of keVs. It is well known that during quiet times, the ring current is dominated by H^+ , while O^+ ion contribution increases significantly during geomagnetically active times and even dominates during very intense storms (Daglis et al., 1999; Greenspan & Hamilton, 2002; Keika et al., 2013; Nose et al., 2005). It has been showed using in situ observations and modeling that during storm times, O^+ ions originating from the ionosphere contribute significantly to the ring current (Daglis et al., 1999; Ebihara et al., 2006; Fok et al., 2001; Kistler et al., 2016; Keika et al., 2018).

It has been found through modelling (Jordanova, 2003; Jordanova et al., 2001) and observation that the ring current is asymmetric during the main and the early recovery phase (Ebihara & Ejiri, 2000; Liemohn et al., 1999, 2001; Ebihara and Miyoshi, 2011; Kumar et al., 2020). This asymmetry can be due to the loss of ions through the dayside magnetopause following their open drift paths, finite drift times and loss processes along the drift paths (Jordanova et al., 1998; Kozyra and Liemohn, 2003). This asymmetry can be different for different species as the charge exchange losses are species dependent (Smith et al., 1981; Jordanova et al., 1996). The ring current is found to be symmetric during the beginning of late recovery phase because of weakening of convection (Li et al., 2011; Kozyra and Liemohn, 2003).

There are various loss processes influencing the intensity of the ring current. Charge exchange with neutral hydrogen of geocorona is one of the main loss processes (Daglis et al., 1999). Other loss processes include, scattering by the plasmaspheric ions and electrons due to Coulomb collisions (Jordanova et al., 1996), pitch angle scattering, wave particle interaction with waves, such as Electromagnetic Ion Cyclotron (Jordanova, 2003; Miyoshi et al., 2008; Summers et al., 2007) and whistler waves (Kozyra et al., 1994). Escape through the dayside

This article is protected by copyright. All rights reserved.

magnetopause (Jordanova et al., 2003; Keika et al., 2005, 2006) and field line curvature scattering also contributes to the loss of ring current particles (Young et al., 2002, 2008; Yu et al., 2020).

There are a variety of geomagnetic indices to measure the geomagnetic activity. Disturbance storm time (Dst) index is widely used, and it primarily represents changes in the magnetic field caused by the ring current, magnetopause currents, tail current (Sugiura, 1964; Sugiura and Kamei, 1991; Daglis and Thorne, 1999; Liemohn et al., 2001). According to the Dessler Parker Sckopke (DPS) relationship (Dessler and Parker, 1959; Sckopke, 1966), the Dst index indicates the total energy stored in the inner magnetosphere. It is found that these currents have different origin and effects at different MLTs (Tsyganenko and Sitnov, 2005).

It is well known that the nightside plasma sheet particles convecting inwards have a significant contribution to the ring current during the main phase of the storm. Some modeling studies have shown that the plasma sheet ions on an open drift path have a significant contribution to the Dst development during the storms (Jordanova et al., 1998, 2003; Ebihara and Ejiri, 1998; Kozyra et al., 2002). It is found that the ions with an energy of <50 keV contribute more significantly to the ring current than those with other energies during the main phase and they even dominate during the late recovery phase and quiet time (Zhao et al., 2015; Keika et al., 2011, 2018). Some statistical studies have shown that the Sym-H (or Dst) depression during the main phase of the storm is very well correlated with <80 keV (governed by convective timescales) particles (Gkioulidou et al., 2016). They also showed that >100 keV protons has no correlation with Sym-H. Temporin and Ebihara (2011) showed that high energy ion fluxes decrease during the main phase and increase during the recovery phase and sometimes exceed the pre-storm level.

It has been shown using observations and modeling that during storm time, O^+ ions from the ionosphere contribute significantly to the ring current (Daglis et al., 1999; Ebihara et al., 2006; Kistler et al., 2016; Yue et al., 2011; Keika et al., 2018). Greenspan and Hamilton (2002) showed statistically that O^+ has contribution around 10-30% to the total ring current and even becomes the dominant species during some intense storms. It was found that the majority of O^+ contribution to the ring current is made by those with energies below 50 keV (Zhao et al., 2015). Yue et al. (2018) found that the ion and electron pressures peak at dusk and dawn, respectively, during disturbed conditions. In addition, they also found that O^+ (<50 keV)

This article is protected by copyright. All rights reserved.

contribute 25% to the pressure on the nightside during the active times. Using Van Allen Probes observations, Mouikis et al. (2019) performed a comparative statistical study for the ring current ion development during ICME and CIR driven geomagnetic storms. They found that the H^+ pressure variation is similar between ICME and CIR driven geomagnetic storms. However, they found that O^+ ion (< 55 keV) response is significantly different for ICME and CIR driven storms. It was found that O^+ pressure peaks at lower L-shells than H^+ and it increases significantly with decreasing L-shell in ICME driven storms.

The ring current ion composition during active and quiet times is well studied using in situ observations and modeling (Daglis et al., 1999; Kistler et al., 1989, 2016; Ebihara et al., 2002; Miyoshi et al., 2006; Jordanova et al., 1996, 1998, 2006, 2012). However, there have been limited studies on the electron contribution to the ring current. Liu et al. (2005) showed that the electron contribution to the ring current during quiet times is $\sim 1\%$ and increases during disturbed times to $\sim 8-19\%$. Yue et al. (2018) found that electrons with energies of < 40 keV contribute 20% to the pressure in the nightside sector during active times. Recently, Kumar et al. (2021) has shown that the electron pressure also contributes ($\sim 12\%$) to the total ring current during a CIR-driven storm, by comparing the Ring current Atmosphere interactions Model with Self Consistent magnetic field (RAM-SCB) simulation, Arase in-situ plasma/particle, and ground-based magnetometer data. It was also shown using modeling that the electron contribution to the ring current reached $\sim 20\%$ during the peak of high-speed stream driven storm (Jordanova et al., 2012). Modeling study by Jordanova and Miyoshi (2005), which included the global drift loss of ions and electrons, predicted that the electron contribution increases to $\sim 10\%$ during active times as compared to quiet times ($\sim 1\%$). It was shown using Van Allen probes observations that the electron contribution to the ring current was $\sim 12\%$ for a moderate storm and it decreases to $\sim 7\%$ for an intense storm (Zhao et al., 2016). The previous studies, however, lacked a detailed statistical examination to demonstrate the electron contribution to the ring current.

It has been found that CIR driven storms drive geomagnetic activity for a longer period, making them more geoeffective as the recovery phase is very long and driven by a series of substorms (Turner et al., 2009; Miyoshi and Kataoka, 2005, 2008; Miyoshi et al., 2013; Tsurutani et al., 2006). During CIR storms, the prolonged substorm activity appears to play a role in the energization of the ring current (Cramer et al., 2013; Sandhu et al., 2018; Katus et al., 2015)

and radiation belts (Miyoshi and Kataoka, 2008). Using geosynchronous observations from Los Alamos National Laboratory-Magnetospheric Plasma Analyzer (LANL-MPA) it was found that CIR driven storms produce the plasma sheet with higher temperatures for the longer period as compared to ICME driven storms (Borovsky and Denton, 2006; Denton et al., 2006). This difference was attributed to the different solar wind drivers.

Plasma pressure of different species in the inner magnetosphere plays an important role in plasma dynamics and generation of electric currents. The knowledge of plasma pressure in the inner magnetosphere is important as it reflects the source, transport and loss of different ion and electron populations. In this work, we investigate statistically for the first time the ring current composition during CIR driven storms by separately evaluating the contribution of ions (H^+ , He^+ , O^+) and electrons using the Arase observations. We perform a superposed epoch analysis to investigate the pressure development of the ions and electrons for different energies during the different phases of storms as well as examine their L-shell and magnetic local time (MLT) distribution. A special attention is given to the electron contribution to the ring current during CIR driven geomagnetic storms.

2. Data Set

The Exploration of energization and Radiation in Geospace (ERG) satellite, also known as Arase, has an elliptical orbit with a perigee of 400 km, an apogee of 32,000 km altitude with an inclination of 31° (Miyoshi et al., 2018a). In the present analysis, we use ion data (H^+ , He^+ , and O^+) obtained from low-energy particle experiments-ion mass analyzer (LEP-i [10 eV/q–25 keV/q]) (Asamura et al., 2018, Asamura et al., 2018a, 2018b), medium-energy particle experiments-ion mass analyser (MEP-i [10–180 keV/q]) (Yokota et al., 2017, Yokota et al., 2018a, 2018b) and the electron data from low-energy particle experiments-electron analyzer (LEP-e [19 eV–20 keV]) (Kazama et al., 2017; Wang et al., 2018a, 2018b), medium-energy particle experiments-electron analyzer (MEP-e [7–87 keV]) (Kasahara et al., 2018; Kasahara et al., 2018a, 2018b) instruments on board Arase satellite.

3. Results

In this study, we analysed 26 CIR driven storms during the Arase period (2017-2021) with minimum Sym-H between -33 and -86 nT (shown in Table 1). Figure 1 shows the interplanetary parameters in Geocentric Solar Magnetospheric coordinates and geomagnetic indices during 26 CIR storms with 1-minute resolution. The variation of solar wind velocity

This article is protected by copyright. All rights reserved.

(V_{sw}), temperature (T_p), solar wind density (N_{sw}), dynamic pressure (P_{dy}), the B_z component of the interplanetary magnetic field, SuperMAG Auroral index (SML), and Sym-H index are shown in Figure 1 from top to bottom (a–g). The dark blue line represents the mean variation. Zero epoch represents the minimum Sym-H. It can be seen from Figure 1a, 1b and 1c that the storms were accompanied by an increase in the solar wind velocity (V_{sw}), temperature (T_p) and a decrease in the solar wind density (N_{sw}) along with enhanced auroral activity shown by SML index (Figure 1f). These are typical characteristics of CIR-driven storm with a long-lasting recovery phase (e.g., Miyoshi & Kataoka, 2008; Miyoshi et al., 2013; Tsurutani et al., 2006). Each storm is divided into different phases based on the Sym-H variation. The shaded red, purple, and green portions show the main phase, early recovery phase and late recovery phase, respectively. The main phase is defined as the period of decrease in Sym-H until the minimum value of Sym-H for each individual storm (t₀). The early recovery phase is marked by t₀+1 day (t₁) from the minimum Sym-H, whereas the late recovery phase is marked as t₁+4 days from the early recovery phase. The prestorm condition refers to geomagnetically quiet periods (Sym H > -20). In this study storms that have a secondary decrease in Sym-H during the recovery phase are not included to avoid the events with disturbed pre-conditions. During the late recovery phase, if Sym-H recovered to the prestorm level before +4 days, the duration until which Sym-H recovered is used as a late recovery phase.

The orbit of Arase satellite during different phases of the storms used in the present analysis in the solar magnetic (SM) coordinates is shown in Figure 2. Figure 2a-2d shows the Arase orbit during the pre-storm, main phase, early recovery phase and late recovery phase periods, respectively. The different phases of the storms are distributed reasonably over all MLT sectors.

The average H⁺ partial pressure variation with L shell versus MLT for 26 CIR driven storms for different energy ranges (a) 0.1-10 keV (b) 10-20 keV (c) 20-50 keV and (d) 50-100 keV is represented in the Figure 3. The four columns in Figure 3 correspond to the four storm phases: prestorm, main phase, early-recovery, and late recovery phase. The L shell range coverage is $2 \leq L \leq 8$, with a resolution of 1 L. The L-shell used in this study is McIlwain's L-parameter (McIlwain, 1961). The MLT resolution is 3 hours in time. The 3-hour MLT resolution was adopted to ensure the continuous coverage of all magnetic local time sectors. Midnight (0 MLT) is to the bottom in each plot. The average pressure (P_{avg}) is calculated for each energy

range from the perpendicular and parallel components of the pressure tensor using a relation from De Michelis et al. (1999).

$$P_{\perp} = \pi \sum_E \sum_{\alpha} \sqrt{2mE} J(E, \alpha) \sin^3 \alpha \Delta E \Delta \alpha \quad (1)$$

$$P_{\parallel} = 2\pi \sum_E \sum_{\alpha} \sqrt{2mE} J(E, \alpha) \cos^2 \alpha \sin \alpha \Delta E \Delta \alpha \quad (2)$$

$$P_{avg} = (2P_{\perp} + P_{\parallel})/3 \quad (3)$$

where E is energy, α is the pitch angle of differential flux $J(E, \alpha)$ and m is the mass of species, ΔE is the energy channel width, and $\Delta \alpha$ is the pitch angle bin width.

Figure 3a and 3b show the partial pressure from H^+ ions with energies of 0.1-10 keV and 10-20 keV respectively, measured by LEP-i onboard Arase. Figure 3c and 3d show H^+ pressure from energies 20-50 keV and 50-100 keV respectively, measured by MEP-i.

It can be seen from Figure 3a, during prestorm conditions, the contribution of H^+ is very small (< 1 nPa). The contribution increased during the main phase; however, it is still not very large. Figure 3b shows the H^+ contribution in the 10-20 keV energy range. There is enhancement in the pressure from dusk to post-midnight through midnight during the main phase of the storms in the L-shell range of $4 < L < 6$. However, there is not much (< 1 nPa) enhancement during the early and late recovery phase. Figure 3c shows the pressure contribution from H^+ with energies of 20-50 keV. During the storm main phase, due to enhanced convection, ions from the plasma sheet are transported inward to lower L shells and are adiabatically energized, contributing to the partial ring current pressure development (Ebihara & Miyoshi, 2011; Kistler et al., 2016). The pressure enhancement can be seen from dusk through post-midnight. There is a clear asymmetry in the H^+ pressure distribution. The pressure enhancement can be seen during the early recovery phase over almost all the MLTs. In the late recovery phase, the H^+ pressure becomes almost symmetric with small enhancements in the 21-03 MLT sector. Figure 3d shows the contribution of H^+ in an energy range of 50-100 keV. In this energy range H^+ has a contribution of ~ 1 nPa and forms a symmetric distribution in MLT during the prestorm. During the main phase, the enhanced pressure can be seen in the 15-03 MLT sector and the ring current is asymmetric. The pressure seems to be more symmetric during the early and late recovery phase. The dayside MLT sectors do not show as large pressure enhancements as the nightside sectors (Figure 3), and this is probably because the magnetopause flow-out loss suppresses the pressure build-up there.

This article is protected by copyright. All rights reserved.

The pressure contribution from He^+ to the ring current for different phases of the storm for all MLTs is shown in Figure 4. Figure 4a and 4b shows the pressure contribution from He^+ with energies of 0.1-10 keV and 10-20 keV, respectively, measured by LEP-i. Figure 4c and 4d shows the pressure contribution from higher energy He^+ ions, 20-50 keV and 50-100 keV, respectively, measured by MEP-i. The pressure variations of He^+ over MLT and L are qualitatively similar to that of H^+ in terms of energy and the storm phase. However, the contribution is very small (~ 0.1 nPa) over all MLT sectors and L-shell range.

The O^+ pressure distribution for the different storm phases for all local times can be seen in Figure 5. Figure 5a and 5b show the pressure contribution from O^+ ions with energies of 0.1-10 keV and 10-20 keV, respectively. Figure 5c and 5d show the contribution from higher energy O^+ of 20-50 keV and 50-100 keV, respectively. In Figure 5a during prestorm the O^+ pressure is very small; however, in the main phase there is a pressure enhancement (~ 1 nPa) in the 21-00 MLT sector. The small pressure enhancement can also be seen during the early recovery phase over a wide range of MLT.

As seen from Figure 5b, the O^+ pressure in the 10-20 keV energy range shows a significant increase during the main phase as compared to the prestorm level. The increased pressure can be seen in the 15-06 MLT regions across midnight. The increased pressure is similar to the H^+ pressure in the same energy range. O^+ and H^+ , if having the same energy, follow the same drift paths from the source, which is most likely to be the nightside plasma sheet, but with different charge exchange lifetimes. However, the O^+ pressure enhancement can be seen at lower L shells ($3 < L < 6$) as compared to the H^+ pressure. The O^+ pressure is highly asymmetric during the main phase. In the early recovery phase, the O^+ pressure is also spread over prenoon and afternoon sectors. In the late recovery phase, the O^+ pressure becomes symmetrical with small magnitudes. Figure 5c shows the O^+ pressure contribution in the 20-50 keV energy range. The O^+ pressure of this energy range is very small during prestorm but in the main phase there is a pressure enhancement at the lower L shells ($3 < L < 5$) in the 18-24 MLT sector. This pressure enhancement can be seen also during the early recovery phase with a wider extent in MLT and L value. The main reason for this enhancement is the convection during the main and early recovery phase.

During the late recovery phase, the O^+ pressure becomes symmetrical with low pressure values as compared to the main and early recovery phase. Figure 5d shows the O^+ pressure in the 50-100 keV energy. The O^+ pressure is asymmetric during the main phase with enhanced pressure in the dusk to midnight region. The enhanced O^+ pressure can be seen over almost all MLT sectors during the early recovery phase. However, the O^+ pressure enhances even more in the dusk sector. In the late recovery phase, the pressure shows a symmetric distribution in MLT, but its magnitude is much smaller than the H^+ pressure in the same energy range.

The electron pressure contribution to the ring current for different phases of the storm for all MLTs can be seen in Figure 6. Figure 6a and 6b show the pressure contribution from electrons with energies of 0.1-10 keV and 10-20 keV, respectively. Figure 6c and 6d show the pressure contribution from electrons in the energy range of 20-50 keV and 50-87 keV, respectively.

During prestorm, there is a weak enhancement of electron pressure at higher L-shells ($7 < L < 8$) in the 00-06 MLT sector (Figure 6a). The pressure increases and extends in MLT and L during the main phase. The peak pressure is located around $L = 6$. The enhanced pressure can be seen in the dusk to morning sector (00-09 MLT) on the nightside as compared to the prestorm condition. In the early recovery phase, the pressure enhancement is spread more in MLT than the main phase. The pressure enhancement can be seen in the 00-12 MLT and 18-24 MLT sectors. The pressure values are smaller than the main phase. The peak pressure is seen in $L = 5.5-6$ and MLT \sim 00-03. During the late recovery phase, the pressure enhancements can be seen in the same MLT sectors as during the early recovery phase but with smaller magnitudes.

The electron pressure (10-20 keV) is larger at higher L shells during prestorm conditions in the midnight to dawn sectors (Figure 6b). In the main phase, the enhanced electron pressure is observed at $L = 5-7$ in the MLT range of 00-06. There is clear asymmetry in the electron pressure. This asymmetry can be observed also during the early and late recovery phase. However, the electron pressure is smaller than that of the main phase, as there is strong convection during the main phase.

The electron pressure in the 20-50 keV energy range is shown in Figure 6c. In the main phase, the pressure increases significantly as compared to the prestorm. The enhanced pressure can be seen in the 00-09 MLT sector. In the early recovery phase, the pressure enhancements can

This article is protected by copyright. All rights reserved.

also be seen in the same sector with some additional enhancements in the 21-24 MLT sector. In the late recovery phase, high electron pressure is seen in the 00-06 MLT sector, whereas it looks uniform in the other MLT sectors.

The electron pressure in the 50–87 keV energy range is shown in Figure 6d. There is an increase in the electron pressure during the main phase of the storm in the 00-09 MLT sector. This pressure contribution is smaller than those of lower energies (<50 keV). In the early recovery phase, this enhancement can be seen in the 03-09 MLT sector. In the late recovery phase, the pressure is small and looks almost uniform in MLT except in 00-06 MLT. Compared to the H^+ pressure that becomes almost symmetric during the late recovery (Figure 3), the electron pressure remains asymmetric even during the late recovery phase.

The total pressure of ions (H^+ , He^+ , O^+) and electrons summed over all the energies shown in Figures 3-6 is calculated and is shown in Figure 7. Figure 7a shows the pressure of H^+ for different phases of the storm. The H^+ pressure is symmetric during the prestorm. In the main phase the pressure is asymmetric with high pressure values in the dusk to midnight sector. The pressure becomes symmetric during the early and late recovery phase. In the late recovery phase, the dayside pressure is smaller than the other sectors.

The He^+ pressure (Figure 7b) is much smaller than the H^+ pressure for all the phases of the storm. During the main phase, there are small pressure enhancements in the dusk sector. The He^+ pressure is not significant in the early and late recovery phases.

There is a significant increase in the O^+ pressure (Figure 7c) in the main phase as compared to prestorm. Later in the main phase, the O^+ pressure becomes asymmetric. The dusk to midnight sector has the highest-pressure enhancements among all MLT sectors. In the early recovery phase, the O^+ pressure looks symmetric and continues to be so even during the late recovery phase, unlike the H^+ pressure.

In the prestorm condition, the electron pressure (Figure 7d) is very small, and a relatively high pressure is confined to the midnight to dawn sector at higher L shells ($L > 7$). In the main phase, electron pressure enhancements can be seen over the 00-09 MLT sector and even in the pre-midnight sector. The high-pressure region expands also toward lower L shells ($L \sim 6$). The electron pressure is highly asymmetric during the main phase. The electron pressure is

This article is protected by copyright. All rights reserved.

asymmetric during the early recovery phase. Compared to the main phase, the electron pressure distribution is extended in MLT through 12 MLT sector, whereas the pressure magnitude is lower. The electron pressure remains highly asymmetric even during the late recovery phase, and the pressure enhancement is found in the 00-06 MLT sectors.

3.1 Energy dependence of ions and electrons in total pressure

The histograms in the left panels of Figure 8 shows the relative contribution for four energy ranges to the energy integrated pressure of (i) H^+ , (ii) O^+ , (iii) He^+ and (iv) electron for the main (blue color), early (red color) and late recovery phase (yellow color) of the storm. Table 2 shows the energy wise contribution of ions and electrons shown in Figure 8. During the main phase, the total H^+ pressure has ~35% contribution from those in the 20-50 keV range. On the other hand, during the early and late recovery phase, the highest contribution comes from those in the 50-100 keV range with a fraction to the total pressure of ~44% and ~54%, respectively.

The total O^+ pressure is dominated by O^+ ions with energies of 10-20 keV, which shows ~42% contribution during the main phase. In the early recovery phase, 20-50 keV O^+ has more contribution (~29%), and in the late recovery phase, again 10-20 keV, O^+ has highest contribution (~44%) to the total O^+ pressure.

The He^+ pressure is mostly dominated by those ions with energies of 50-100 keV for all the phases of the storm (see Table 2). The low energy 0.1-10 keV electrons have the major contribution (~32%) to the total electron pressure during the main phase. The electrons with energies of 20-50 keV dominate the total electron pressure during the early recovery and late recovery phases, with a relative contribution of ~32%.

3.2 MLT and L dependence of the total pressure

The MLT dependence of the total pressure for H^+ , He^+ , O^+ and electrons during the main, early recovery and late recovery phase is depicted in Figure 9 a-c. The rows in Figure 9 (i-iv) show the different MLT sectors. Table 3 summarizes the MLT dependence of the total pressure for ions and electrons during different phases of the storm.

Table 3 shows that H^+ has the highest contribution to the total pressure in all MLTs during all the phases of the storm. In 03-09 MLT, during the main phase, H^+ has ~69% contribution to the total pressure, which is the least in all the MLTs. The H^+ contribution increased

This article is protected by copyright. All rights reserved.

significantly during the late recovery phase in all MLTs. The O^+ has the maximum contribution to the total pressure in the 15-21 MLT sector, $\sim 14\%$ and $\sim 16\%$ in the main and early recovery phase respectively. In the late recovery phase, O^+ contribution decreases in the 15-21 MLT sector to $\sim 7\%$. The He^+ pressure has very little contribution to the total pressure $\sim 2\%$ during all MLTs and all the phases of the storm.

Interestingly, electrons have a significant contribution to the total pressure in 03-09 MLT sector: $\sim 22\%$ during the main phase and $\sim 20\%$ during the early recovery phase (Table 3). In this sector, the electron still has $\sim 13\%$ contribution even in the late recovery phase. In addition, electron has non-negligible contribution $\sim 11\%$, $\sim 12\%$ during main and early recovery phase respectively in the 21-03 MLT sector.

The average pressure variation of H^+ , He^+ , O^+ and electrons with L-value and MLTs is shown in Figure 10. Figure 10a shows the H^+ pressure variation with L-value. The prestorm pressure (black dotted lines) peaks around the $L = 5-6$. The pressure peaks at lower L shells between 4 and 5 during the main, early recovery and late recovery phase. Figure 10b shows the He^+ pressure variation with L value. It shows a similar variation to H^+ pressure with a peak in $L = 4-5$ during storm time. Figure 10c shows the O^+ pressure variation with L value. The pressure during the prestorm time is very small as compared to the storm time. However, pressure peaks at lower shells between 3 and 4 during the main and early recovery phase. Figure 10d shows the electron pressure variation with L-shell. The prestorm electron pressure peaks at a higher L shell around 7. The electron pressure peaks in $L = 5-6$ during the main, early recovery and late recovery phase. Figure 10 e-g shows the average pressure variation of H^+ , He^+ , O^+ with MLT. The ions have pressure peaks in the dusk sector (15-21 MLT) during the main, early recovery and late recovery phase. Figure 10h shows the average electron pressure variation with MLT. The electron pressure peaks in the pre-dawn sector (03 MLT).

4. Summary and Discussion

In this study, we performed a superposed epoch analysis to investigate the average profile of the pressure contribution of the ions (H^+ , He^+ and O^+) and electrons as a function of MLT and L-shell in the ring current development during CIR driven storms. The storm was divided into three different phases: the main, early recovery and late recovery phase. The period when there was no storm is referred to as a prestorm. We used 26 CIR driven storms with minimum Sym-H between -33 and -86 nT.

This article is protected by copyright. All rights reserved.

The prestorm H^+ ($>20\text{keV}$) average pressure is found to be symmetric in MLTs and the peak is seen at $L > 5$ (Figure 3). It is found that the H^+ pressure is highly asymmetric during the main phase. The H^+ with energies of 20-50 keV has a significant contribution during the main phase (Figure 8). The H^+ pressure was asymmetric even during the early recovery phase except for 50-100 keV energy. In the late recovery phase, H^+ pressure decreases to the prestorm level for $< 50\text{keV}$ energy. In the late recovery phase, high energy (50-100 keV) H^+ contributed more to the total pressure. Due to enhanced convection, the pressure enhancements can be seen at a lower L shell ($L = 4$) in the pre-midnight to dusk sector during main and early recovery phase. The nightside plasma sheet is the source of these particles. The dayside shows smaller pressure enhancements as compared to other MLT sectors. This is due to the magnetopause flow-out losses (Keika et al., 2005, 2006 and references therein). The 50-100 keV energy H^+ pressure seems to be symmetric during the late recovery phase (Figure 3). It is found that the high energy ions, especially H^+ pressure contribution to the ring current is fully symmetric during recovery phase and quiet days (Mouikis et al., 2019, Zhang et al., 2011; Temporin and Ebihara, 2011). H^+ is the major contributor to the total ring current during all phases of the storm (Figure 8 and 9). H^+ has the highest contribution to the total ring current $\sim 80\%$ in the 09-21 MLT sector. The dominant contribution of H^+ to the total ring current is consistent with the previous studies.

The He^+ average pressure contribution to the ring current is found to be very small. The low energy ($<50\text{ keV}$) He^+ contribution is $\sim 0.1\text{ nPa}$ during all phases of the storm. The He^+ pressure in the 50-100 keV range has a peak contribution around $\sim 0.4\text{ nPa}$ during the main and early recovery phase. The average He^+ pressure shows similar enhancements spatially in L/MLT as the H^+ pressure enhancements. However, He^+ pressure contribution to the total ring current is found to be very small ($\sim 2\%$) during all the phases of the storm across all MLTs (Figures 8 and 9). Van Allen Probes observations also have shown that the He^+ contribution to the total ring current pressure is generally very small (Yue et al., 2018).

The average O^+ pressure during prestorm is very small. The O^+ pressure increases during the magnetic storms. A significant enhancement is seen in the O^+ ions with energies of 10-20 keV in 06-21 MLT sectors during the main and early recovery phase. In the late recovery phase, O^+ with energies of 10-20 keV contribute more as compared to other energies (Figure 8). It is also to be noted that the O^+ pressure enhancement is different in L-shell as compared to the H^+ pressure enhancements. O^+ pressure enhancements during the main and early recovery phase

This article is protected by copyright. All rights reserved.

can be seen at $L < 4$. Jahn et al. (2017) found that warm O^+ ions dominate closer to the plasmapause and warm H^+ ions are the primary contributor to the ring current pressure at higher L -shells. The O^+ pressure enhancement at lower L -shells may suggest an inner source of O^+ as the drift trajectory depends on energy not on the mass. Menz et al., (2017) found that during a particular storm two effects occurred: firstly, when convection increases the O^+ in the plasma sheet is most enhanced, secondly if the O^+/H^+ ratio at lower energies is higher in the plasma sheet, O^+ gets energized as they drift inwards, and its pressure enhances for lower energies. The O^+ pressure contribution to the total ring current pressure is $\sim 10\%$ during the main and early recovery phase (Figure 8). This contribution increases to $\sim 16\%$ in the 15-21 MLT sector (Figure 9). The O^+ contribution is found to be larger during the intense storms driven by ICMEs (Daglis et al., 1999; Ebihara et al., 2006; Kistler et al., 2016; Keika et al., 2018, Greenspan and Hamilton, 2002).

The average electron pressure shows significant enhancement during main, early recovery and late recovery phase. The low energy electrons 0.1-10 keV show enhancement from evening through morning (Figure 6). During the main and early recovery phase, the electron pressure enhancements can be seen in 00-09 MLT sectors. Interestingly, electron enhancement can still be seen during the late recovery phase in the 00-06 MLT sector. It is well known that CIR driven storms can drive geomagnetic activity over several days due to Alfvén waves associated with the CIRs (Turner et al, 2009; Tsurutani et al., 2006; Miyoshi et al., 2013) and continuous injections are expected during the prolonged substorms (Tsurutani et al., 2006).

The electrons with energies of 0.1-10 keV contribute more to the total electron pressure during the main phase (Figure 8). The electron with energy 20-50 keV has more contribution during the early recovery and late recovery phase. The electron pressure shows asymmetry during all the phases of the storm. As the geomagnetic activity increases, electrons can be lost through the magnetopause depending on drift paths and precipitation to the atmosphere through wave particle interaction (Fok et al., 1991; Ebihara and Miyoshi, 2011; Ni et al., 2014; Jordanova et al., 2012). The electron contribution to the total ring current is found to be $\sim 11\%$ during the main and early recovery phase. In the late recovery phase, the electron contribution is $\sim 9\%$ to the total pressure summed over all species (Figure 8). However, the electron contribution increases significantly in the pre-dawn to morning sector (03-09 MLT) to $\sim 22\%$ during the main and early recovery phase.

The electrons exhibit a non-negligible contribution of ~13% even during the late recovery phase in this sector. Previous studies using Van Allen Probes have shown electrons with 0.1-40 keV contribute ~20% to the total pressure on the nightside during active times (Yue et al., 2018). Zhao et al., 2016 has shown that electrons with < 35 keV contribute around ~30% to the total ring current pressure during a moderate storm. Zhao et al. (2016) also reported that the electron pressure was higher from midnight to dawn as compared to the noon and dusk sectors. Kumar et al. (2021) has also shown that the electron contribution to the total pressure during a particular CIR driven storm was ~18% in the dawn sector.

Previous studies lack of detailed statistical analysis of electron contribution as a function of energy, radial distance and MLT. This study provides for the first time the comprehensive analysis of the electron contribution to the ring current as a function of L-shell, MLT and energy during different phases of the CIR driven storm. In future, we will conduct the similar investigations for the intense storms driven by CMEs.

5. Conclusions

In this paper we have performed a detailed statistical study of plasma pressure distribution and the relative contributions from ions (H^+ , He^+ and O^+) and electrons with different energies during CIR driven magnetic storms using Arase satellite. We divided the storm into three different phases: the main, early recovery and late recovery phase. Our main conclusions from this study are as follows:

1. In agreement with previous studies, the pressure of ions and electrons increases during the main phase of the storm compared to prestorm. The pressure of the ion species peak in the dusk sector whereas the electron pressure peaks in the dawn sector. Therefore, a strong dawn dusk asymmetry can be seen during the main and early recovery phase of the storm.
2. H^+ is the major contributor (~80%) to the total pressure during all phases of the storm. H^+ with energy 20-50 keV has a significant contribution during the main phase. The high energy H^+ (50-100 keV) contributed more during the early and late recovery phase of the storm.
3. O^+ ions with energy 10-20 keV contributed more during the main phase and late recovery phase of the storm. The O^+ contributed ~10% to the total pressure during the main and early

recovery phase. In the dusk sector (15-21 MLT) O^+ contribution increases to $\sim 16\%$. He^+ contribution is found to be very small ($\sim 2\%$) during all the phases of the storm.

4. The electrons with energy 0.1-10 keV and 20-50 keV contributed more during the main phase and early recovery phase. The electron contribution to the total pressure is found to be $\sim 11\%$ during the main and early recovery phase. This contribution is found to be $\sim 22\%$ at 03-09 MLT sector during the main and early recovery phase. This shows the electrons play an important role in the buildup of the ring current in the dawn to morning sector during the main phase and the early recovery phase when many injections occur.
5. The H^+ and He^+ pressure peaks between $L=4$ to 5 during the active time. O^+ pressure peaks at lower L shell ($L=3$ to 4). Electron pressure peaks around $L=5$ and 6.

In this paper we presented the plasma pressure distribution of various ions and electrons as a function of L shell, MLT for different phases of the storm. It is found that electrons contribute significantly ($\sim 22\%$) to the total pressure in 03-09 MLT sector during CIR driven storms. Therefore, in addition to the ion pressure, storm time electron pressure contributes to the build-up of ring current.

Acknowledgments

This study is supported by JSPS-grants 22F22329, 20H01959, 22KK0046, 22K21345, 23H01229. Work at Los Alamos was conducted under the auspices of the US Department of Energy with partial support from NASA grant 80HQTR21T0008. The authors thank Bo-Jhou Wang at ASIAA, Taipei for providing valuable help in LEP-e data onboard Arase.

Open Research

Data Availability Statement

Arase satellite datasets for this research are available in these in-text data citation references: Asamura et al., 2018a, 2018b, Wang et al., 2018a, 2018b, Kasahara et al., 2018a, 2018b, Yokota et al., 2018a, 2018b and Miyoshi et al., 2018c obtained from the ERG Science Center operated by ISAS/JAXA and ISEE/Nagoya University (<https://ergsc.isee.nagoya-u.ac.jp/index.shtml.en>, Miyoshi, et al., 2018b). Science data of the ERG (Arase) satellite in the present study analyzed LEP-i v03_00, LEP-e L2 v02_02, MEP-e-L2 v01_02, MEP-i L2 v01_03, and orbit L2 v02 data. 1-minute solar wind and interplanetary magnetic data were

This article is protected by copyright. All rights reserved.

provided by NASA's CDAWeb (<https://cdaweb.gsfc.nasa.gov/>). SuperMAG indices used in this study were derived from ground magnetometer data provided by many organizations and institutes as listed at <https://supermag.jhuapl.edu/info/?page=acknowledgement>. The SuperMAG indices are available at <https://supermag.jhuapl.edu/>.

Table 1. List of CIR-Driven Magnetic Storms used in the present analysis.

Sr no.	Storm date	Main phase onset	Sym-H
1	2017-03-27	01:04	-86
2	2017-08-31	06:45	-57
3	2017-09-27	06:36	-74
4	2017-11-07	04:37	-89
5	2017-11-20	17:34	-60
6	2017-12-04	16:17	-47
7	2018-04-20	00:28	-86
8	2018-05-05	14:18	-66
9	2018-06-25	09:15	-48
10	2018-09-10	10:52	-64
11	2018-09-21	21:51	-49
12	2018-10-07	10:45	-56
13	2018-11-04	09:55	-66
14	2019-02-27	10:44	-45
15	2019-08-05	03:15	-64
16	2019-08-30	21:36	-63
17	2019-09-27	10:42	-61
18	2019-10-24	09:24	-55
19	2020-02-17	16:26	-46
20	2020-09-24	05:19	-66
21	2020-10-23	17:44	-49
22	2021-01-11	13:59	-54
23	2021-02-06	23:59	-39
24	2021-02-28	23:59	-79
25	2021-03-20	04:55	-59
26	2021-06-15	12:37	-33

Table 2. Energy wise percentage contribution of ions (H^+ , O^+ , He^+) and electrons to the total pressure of that species during the main phase, early recovery, and late recovery phases of the storms

Energy wise % contribution to the total pressure of each species					
Phase of the storm	Energy range (keV)	H^+	O^+	He^+	electron
Main phase	0.1-10	10	10	13	32
	10-20	25	42	29	21
	20-50	35	25	22	26
	50-100 / 50-87	30	23	36	21
Early recovery	0.1-10	10	15	17	23
	10-20	16	28	24	21
	20-50	30	29	20	32
	50-100 / 50-87	44	28	39	24
Late recovery	0.1-10	6	17	11	21
	10-20	14	44	24	22
	20-50	26	22	19	32
	50-100 / 50-87	54	17	46	25

Table 3. MLT wise percentage contribution of ions (H^+ , O^+ , He^+) and electrons to the total pressure during the main phase, early recovery, and late recovery phases of the storms

MLT wise % contribution to the total pressure					
Phase of the storm	MLT	H^+	O^+	He^+	electron
Main phase	03-09	69	7	2	22
	09-15	85	7	2	6
	15-21	80	14	2	4
	21-03	76	11	2	11
Early recovery	03-09	70	9	1	20
	09-15	77	12	2	9
	15-21	78	16	2	4
	21-03	78	9	1	12
Late recovery	03-09	80	6	2	13
	09-15	86	6	2	6
	15-21	88	7	1	4
	21-03	84	6	1	9

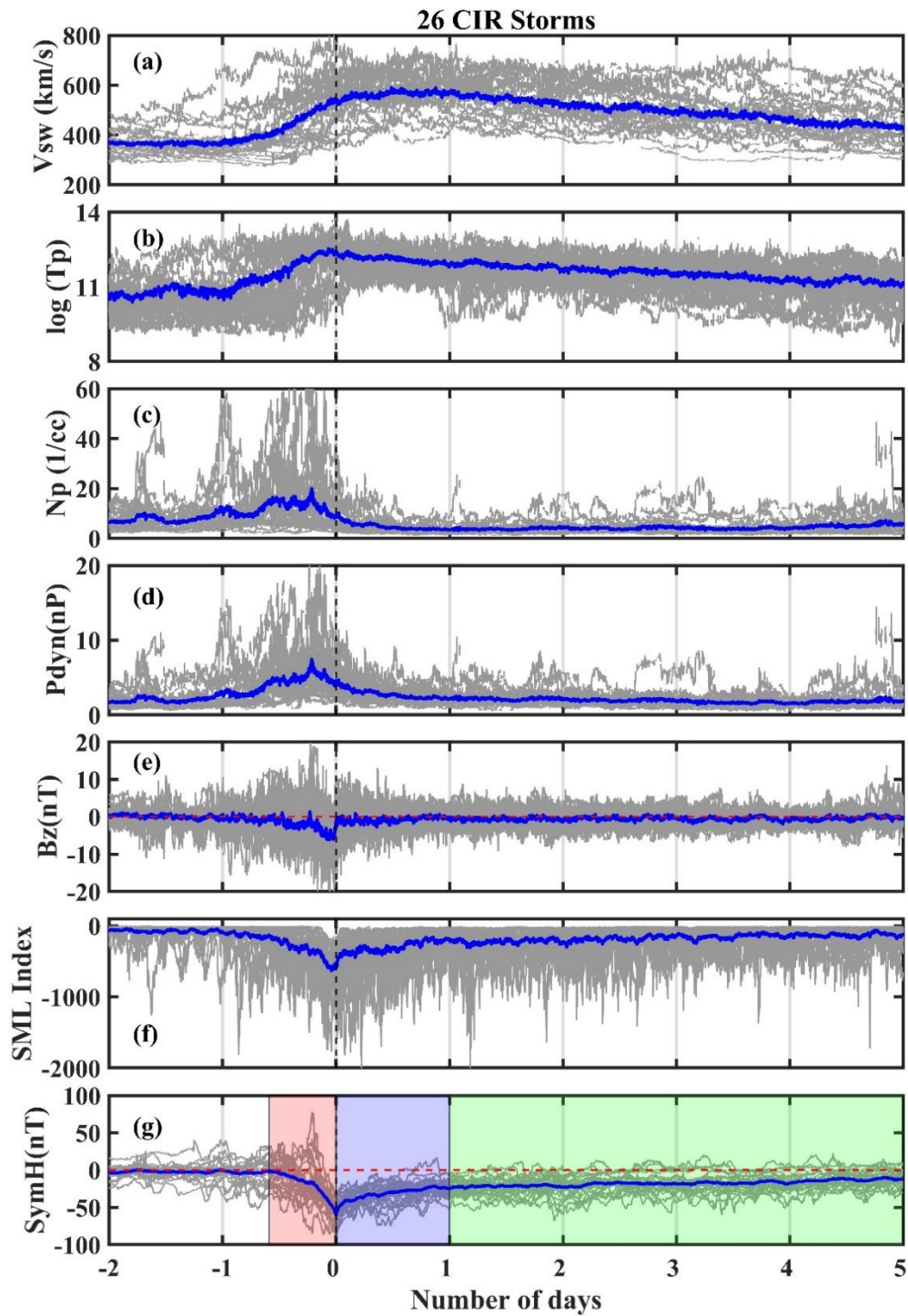


Figure 1. Superposed epoch analysis of 26 CIR storms observed during March 2017-December 2021. (a) solar wind velocity (V_{sw}), (b) solar wind temperature (T), (c) solar wind density (N_{sw}) (d) solar wind dynamic pressure (P_{sw}), (e) interplanetary magnetic field B_z , (f) SuperMAG Auroral Electrojet index (SML), and (g) Sym-H. Zero epoch represents the minimum of Sym-H. Blue lines are the mean of 26 storms. Red, purple and green shaded portions show the main phase, early recovery phase and late recovery phase respectively.

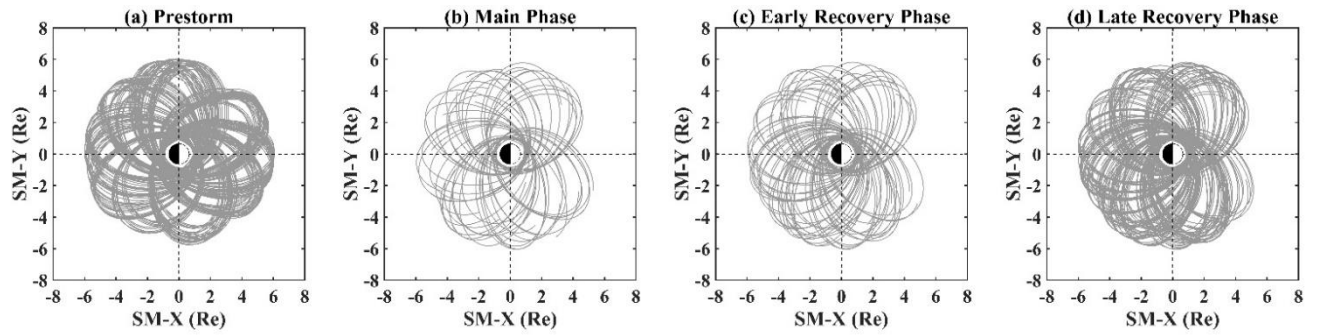


Figure 2. Orbit of the Arase satellite in solar magnetic (SM) coordinates during different phases of the storms (a) Prestorm (b) Main phase (c) Early recovery phase and (d) Late recovery phase.

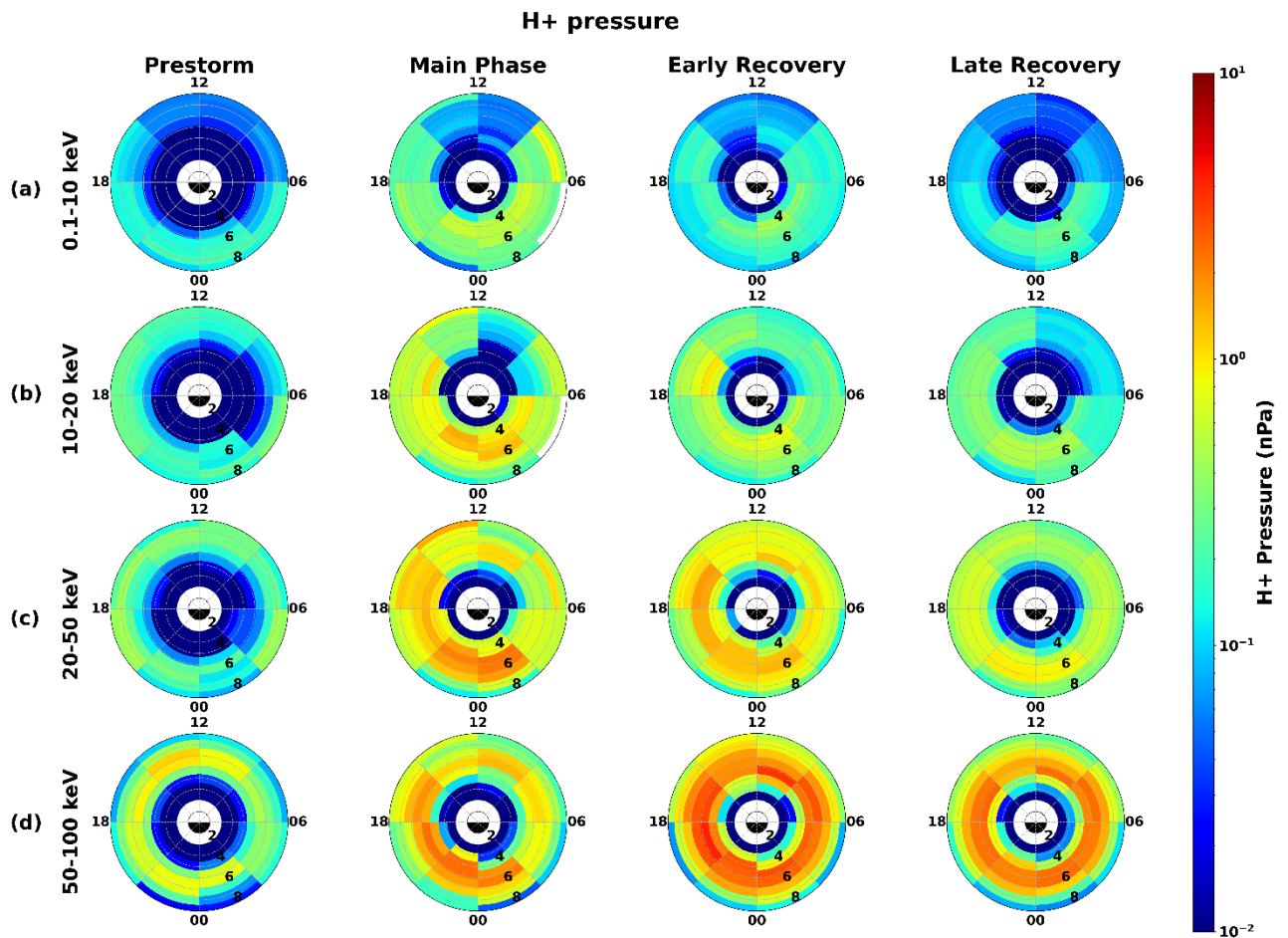


Figure 3. Average variation of H^+ pressure with L-shell and MLT for different energies (a) 0.1-10 keV (b) 10-20 keV (c) 20-50 keV and (d) 50-100 keV during prestorm, main phase, early recovery phase and late recovery phase.

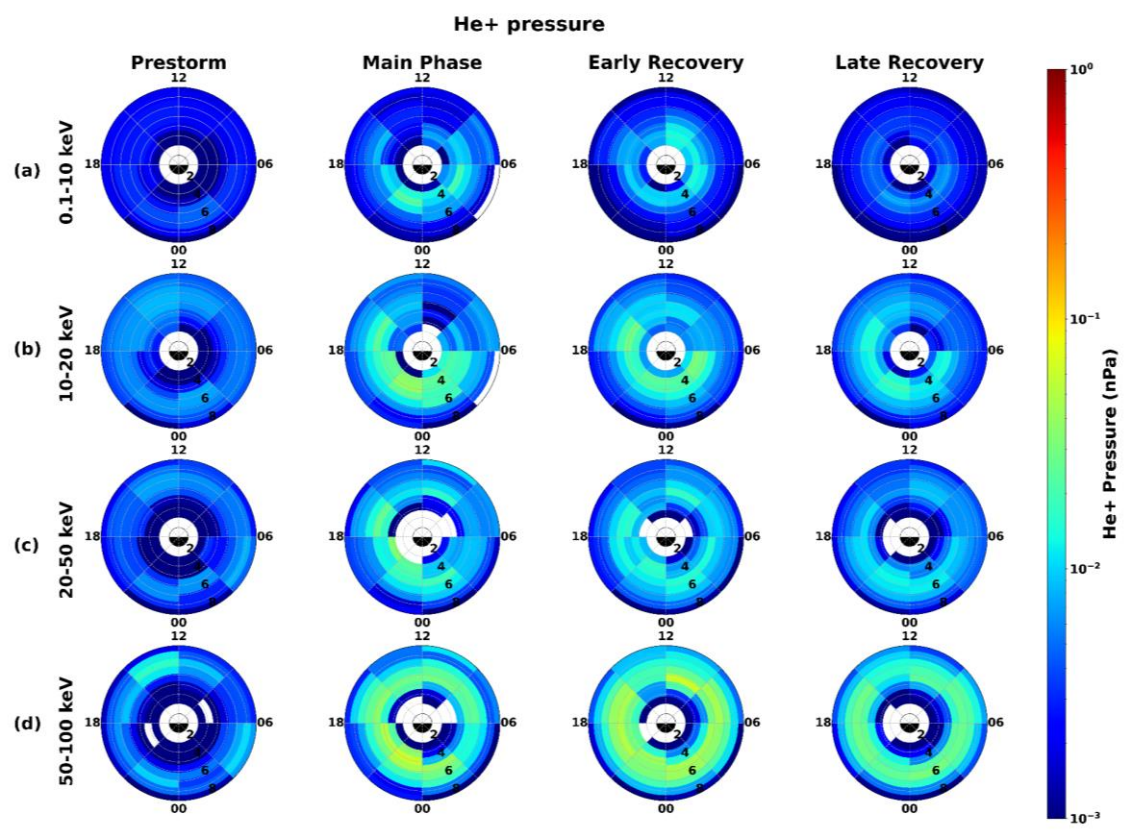


Figure 4. Average variation of He^+ pressure with L-shell and MLT for different energies (a) 0.1-10 keV (b) 10-20 keV (c) 20-50 keV and (d) 50-100 keV during prestorm, main phase, early recovery phase and late recovery phase.

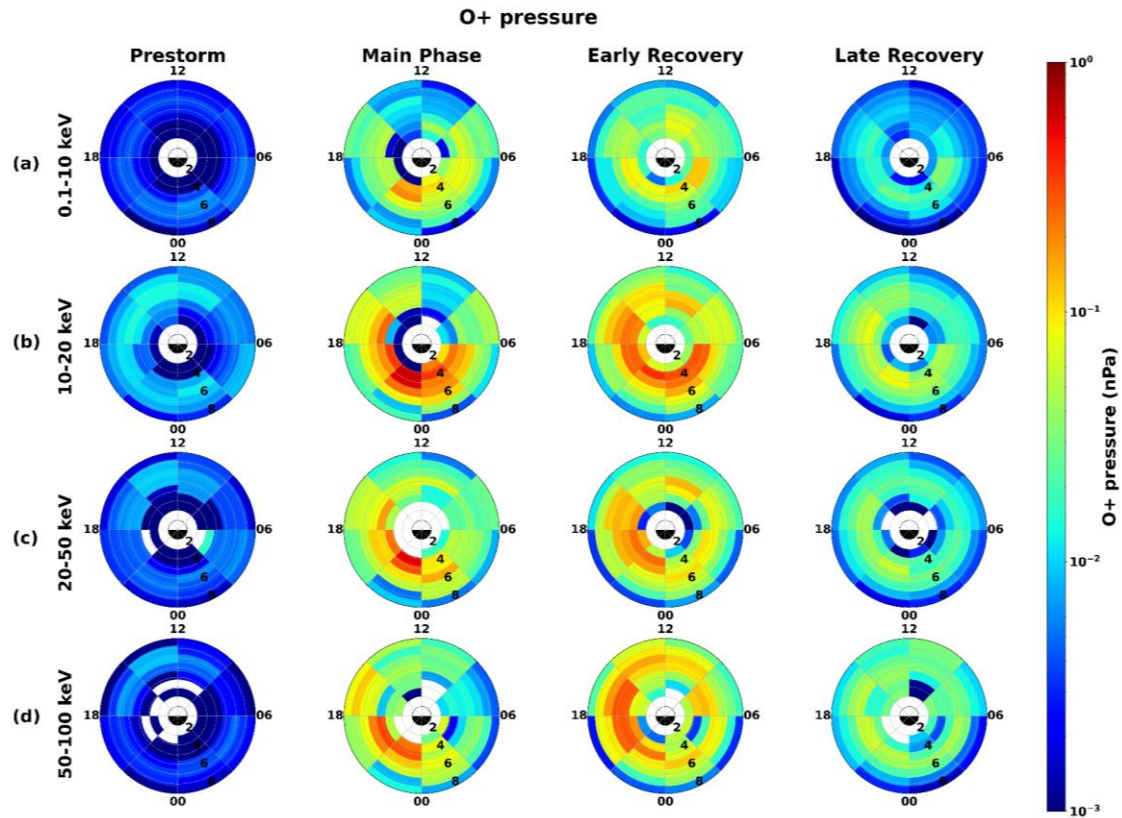


Figure 5. Average variation of O⁺ pressure with L-shell and MLT for different energies (a) 0.1-10 keV (b) 10-20 keV (c) 20-50 keV and (d) 50-100 keV during prestorm, main phase, early recovery phase and late recovery phase.

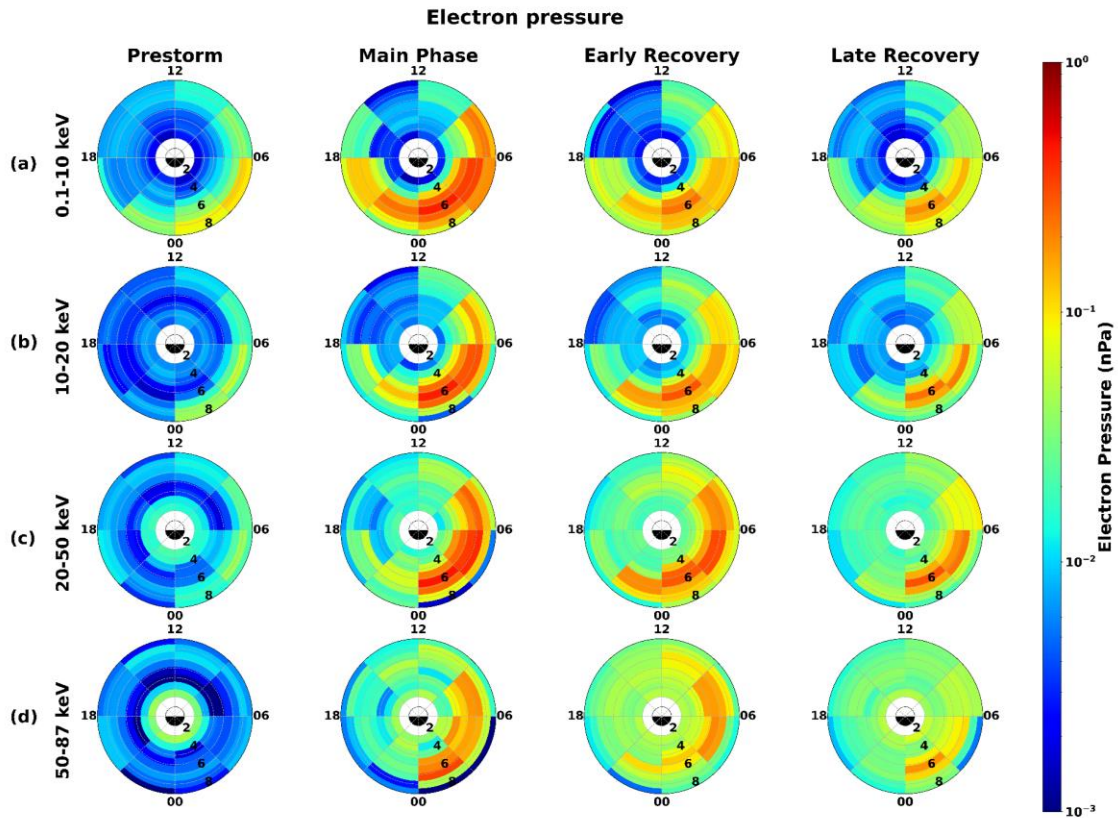


Figure 6. Average variation of electron pressure with L-shell and MLT for different energies (a) 0.1-10 keV (b) 10-20 keV (c) 20-50 keV and (d) 50-100 keV during prestorm, main phase, early recovery phase and late recovery phase.

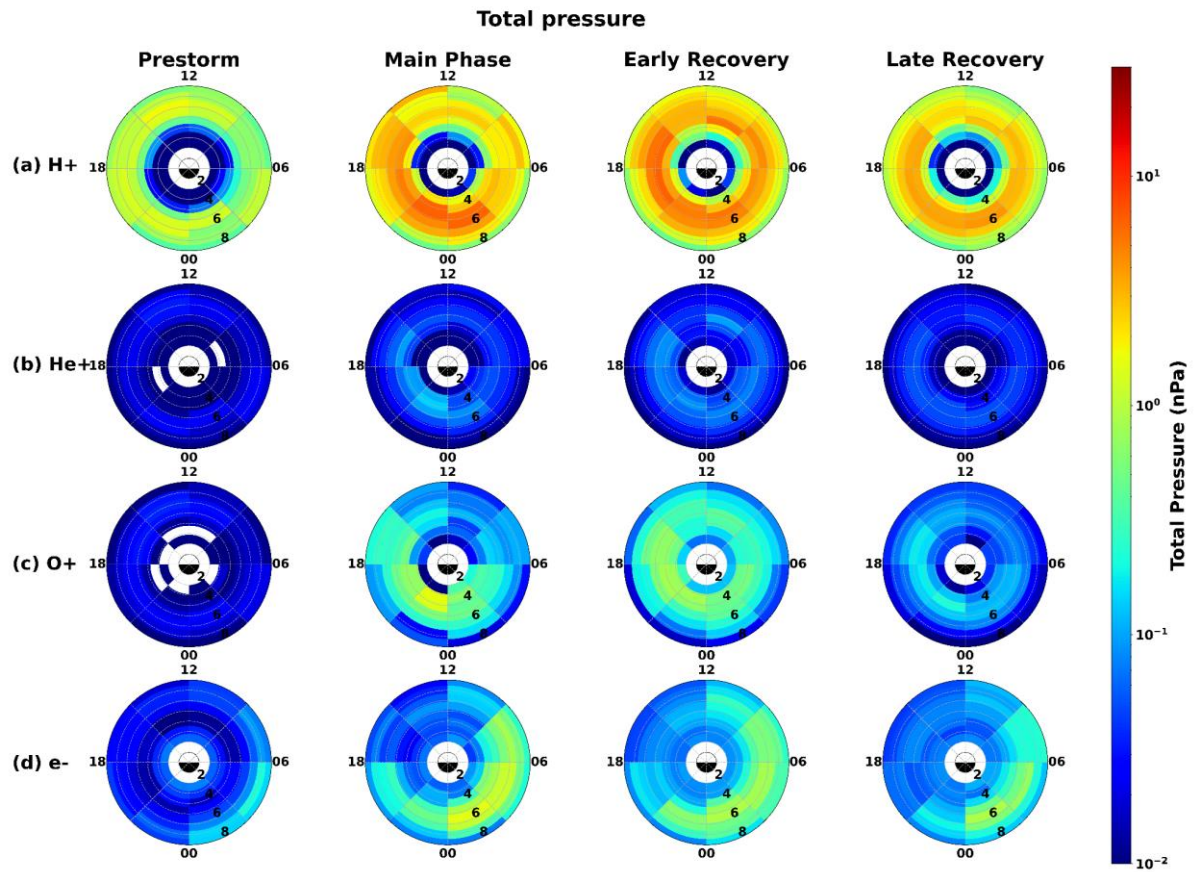


Figure 7. Average variation of total pressure with L-shell and MLT for all different energies during prestorm, main phase, early recovery phase and late recovery phase.

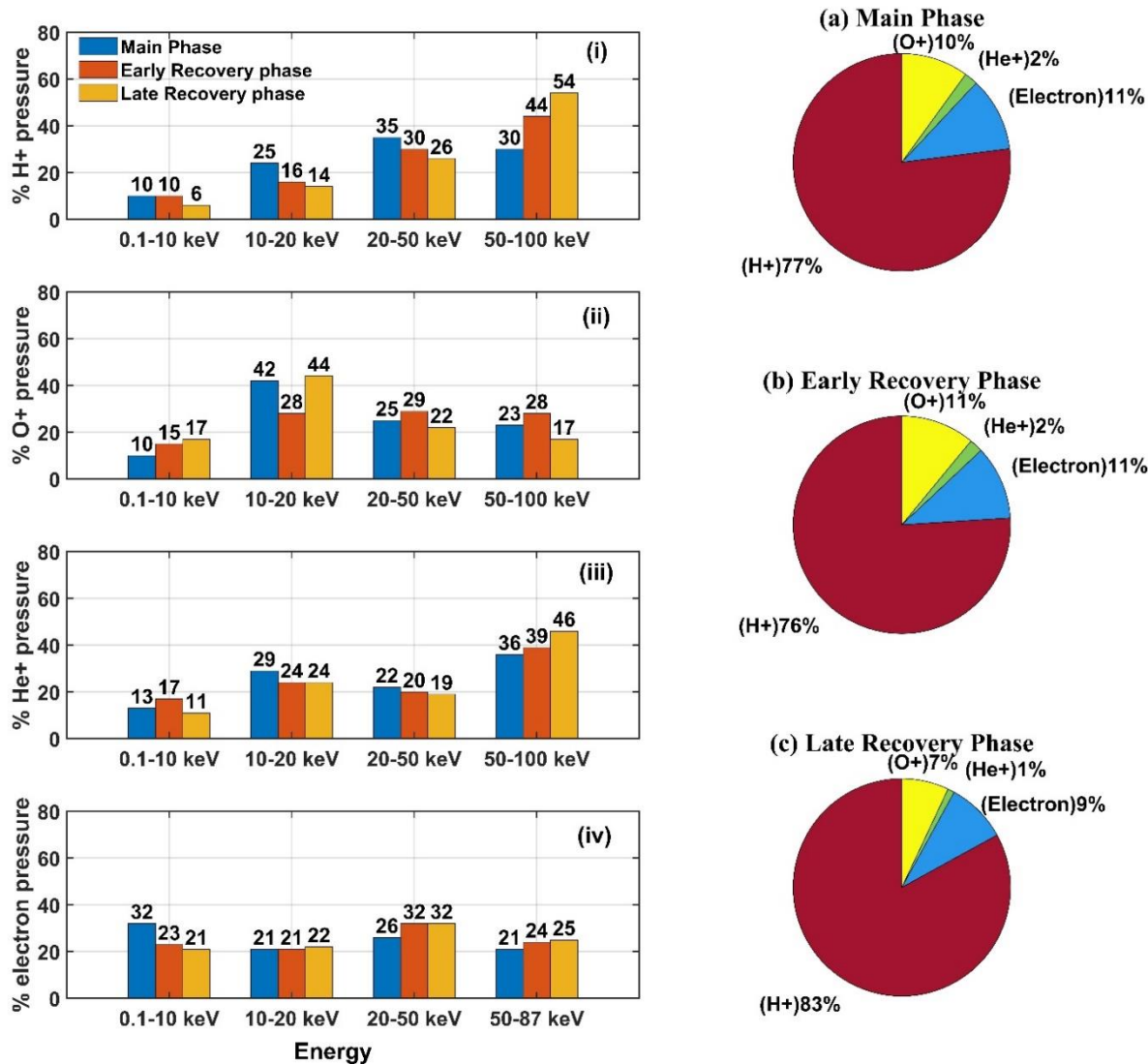


Figure 8. Left panel (i-iv) shows the energy dependence of H⁺, He⁺, O⁺ and electron pressure during main phase, early and late recovery phases of the storm. Right panel (a-c) shows the contribution of H⁺, He⁺, O⁺ and electron pressure to the total pressure during main, early, and late recovery phase.

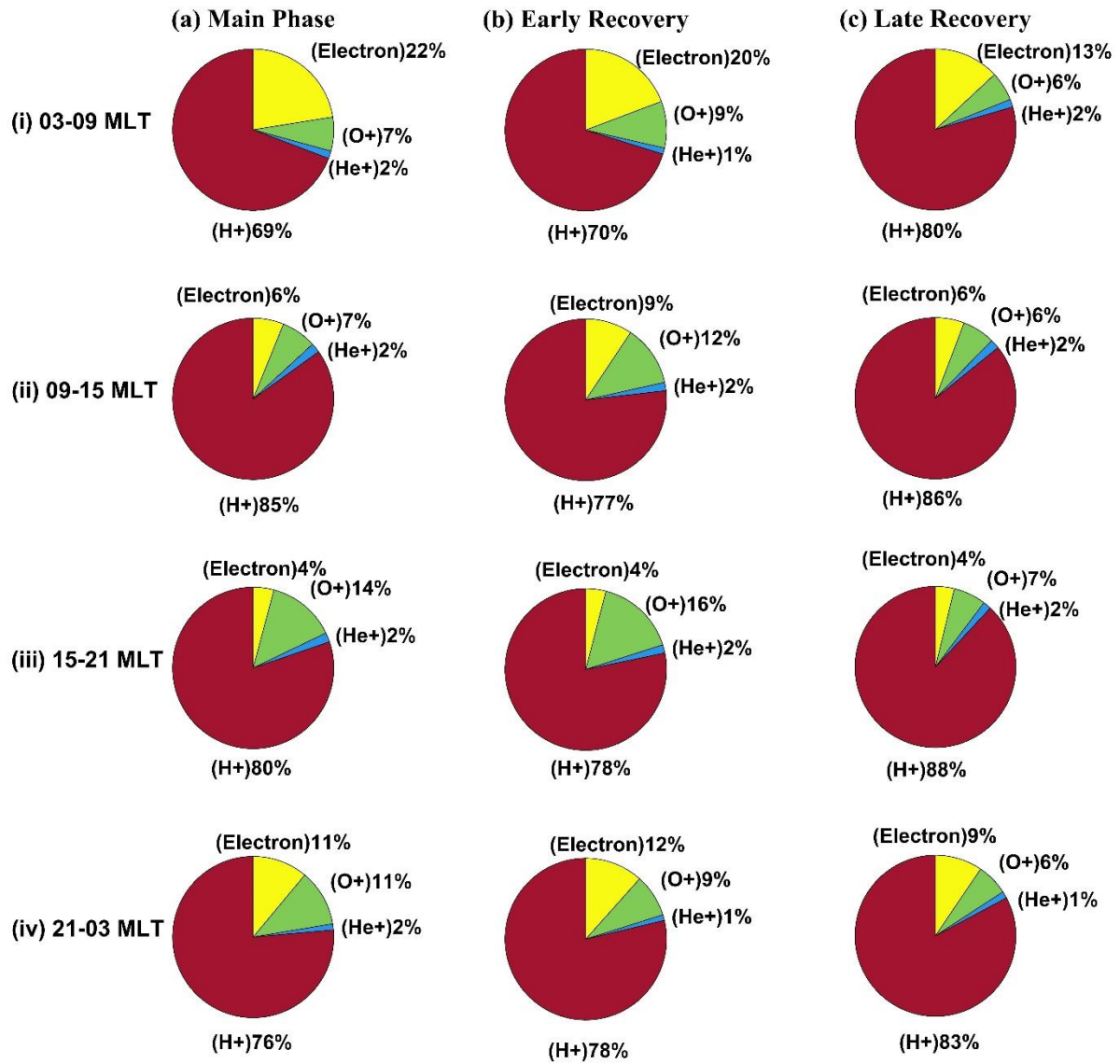


Figure 9. Panel (a-c) shows the contribution of H^+ , He^+ , O^+ and electron pressure to the total pressure during main, early, and late recovery phase for different MLTs sector (i) 03-09 MLT, (ii) 09-15 MLT (iii) 15-21 MLT and (iv) 21-03 MLT.

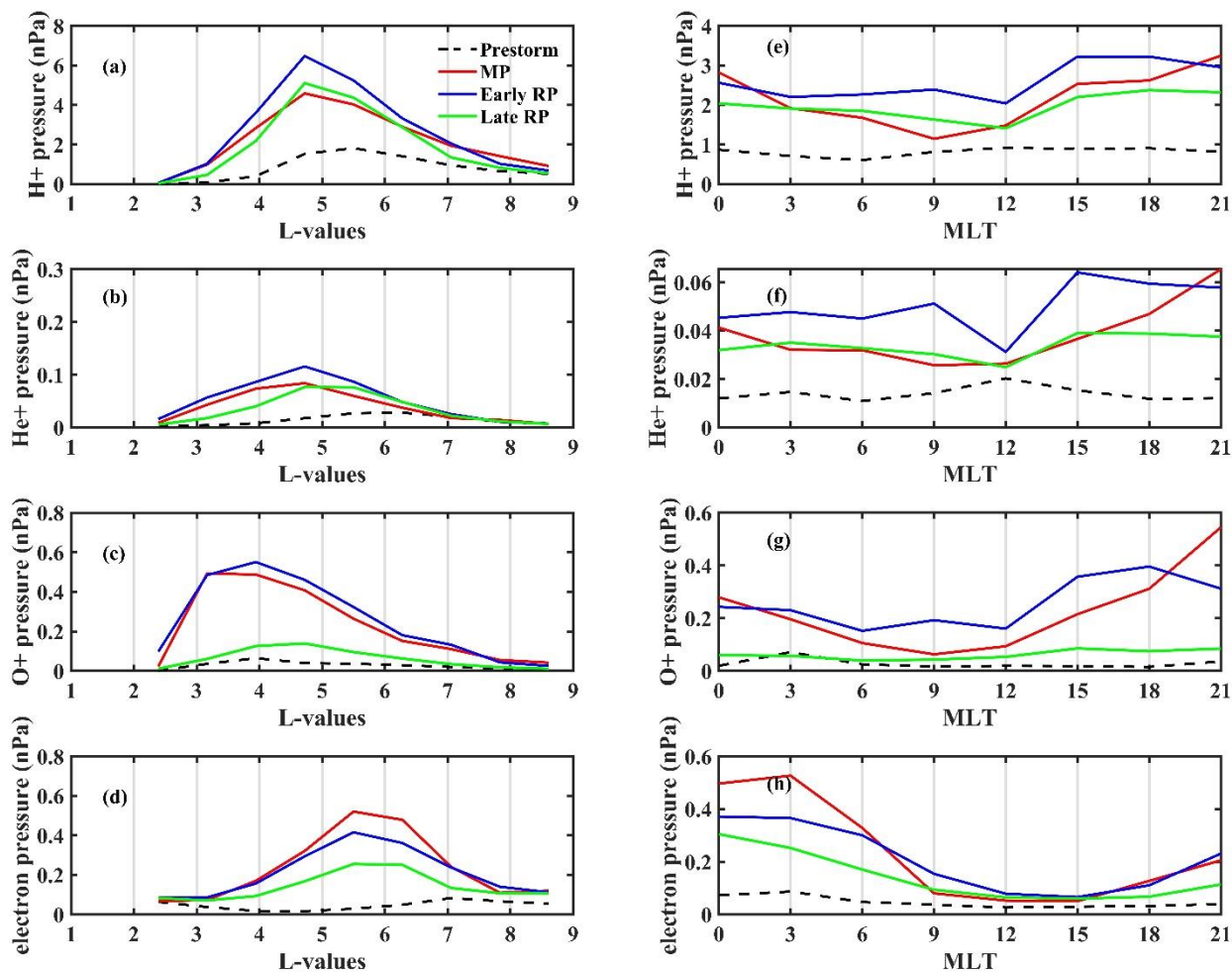


Figure 10. Left panel from (a)-(d) shows the pressure variation with L- values for H⁺, He⁺, O⁺ and electron respectively. Right panel shows the pressure variation with MLT for H⁺, He⁺, O⁺ and electron respectively.

References:

- Alves, M. V., E. Echer, and W. D. Gonzalez (2006), Geoeffectiveness of corotating interaction regions as measured by Dst index, *J. Geophys. Res.*, 111, A07S05, <https://doi.org/10.1029/2005JA011379>.
- Asamura, K., Kazama, Y., Yokota, S., Kasahara, S., & Miyoshi, Y. (2018). Low-energy particle experiments-ion mass analyzer (LEPi) onboard the ERG (Arase) satellite. *Earth, Planets and Space*, 70, 70. <https://doi.org/10.1186/s40623-018-0846-0>.
- Asamura, K., Miyoshi, Y., & Shinohara, I. (2018a). *The LEPi instrument Level-2 3-D flux data of Exploration of energization and Radiation in Geospace (ERG) Arase satellite, Version v03_00*. [Dataset]. ERG Science Center, Institute for Space-Earth Environmental Research, Nagoya University. <https://doi.org/10.34515/DATA.ERG-05001>.
- Asamura, K., Miyoshi, Y., & Shinohara, I. (2018b). *The LEPi instrument Level-2 omniflux data of Exploration of energization and Radiation in Geospace (ERG) Arase satellite, Version v03_00*. [Dataset]. ERG Science Center, Institute for Space-Earth Environmental Research, Nagoya University. <https://doi.org/10.34515/DATA.ERG-05000>.
- Borovsky, J. E., & Denton, M. H. (2006). Differences between CME-driven storms and CIR-driven storms. *Journal of Geophysical Research*, 111, A07S08. <https://doi.org/10.1029/2005JA011447>.
- Burlaga, L., E. Sittler, F. Mariani, and R. Schwenn (1981), Magnetic loop behind an interplanetary shock: Voyager, Helios, and IMP 8 observations, *J. Geophys. Res.*, 86, 6673–6684, <https://doi.org/10.1029/JA086iA08p06673>.
- Cramer, W. D., Turner, N. E., Fok, M. C., & Buzulukova, N. Y. (2013). Effects of different geomagnetic storm drivers on the ring current: CRCM results. *Journal of Geophysical Research: Space Physics*, 118, 1062–1073. <https://doi.org/10.1002/jgra.50138>.
- Daglis, I. A., and R. M. Thorne (1999), The terrestrial ring current: Origin, formation, and decay, *Rev. Geophys.*, 37, 407–438, <https://doi.org/10.1029/1999RG900009>.
- Daglis, I. A., Thorne, R. M., Baumjohann, W., & Orsini, S. (1999). The terrestrial ring current: Origin, formation, and decay. *Reviews of Geophysics*, 37(4), 407–438. <https://doi.org/10.1029/1999RG900009>.
- De Michelis, P., Daglis, I. A., & Consolini, G. (1999). An average image of proton plasma pressure and of current systems in the equatorial plane derived from AMPTE/CCE-CHEM measurements. *Journal of Geophysical Research*, 104(A12), 28615–28624. <https://doi.org/10.1029/1999JA900310>.

Denton, M. H., Borovsky, J. E., Skoug, R. M., Thomsen, M. F., Lavraud, B., Henderson, M. G., et al. (2006). Geomagnetic storms driven by ICME and CIR dominated solar wind. *Journal of Geophysical Research*, 111, A07S07. <https://doi.org/10.1029/2005JA011436>.

Dessler, A. J., and E. N. Parker (1959), Hydromagnetic theory of geomagnetic storms, *J. Geophys. Res.*, 64, 2239. <https://doi.org/10.1029/JZ064i012p02239>.

Dmitriev, A. V., N. B. Crosby, and J.-K. Chao (2005), Interplanetary sources of space weather disturbances in 1997 to 2000, *Space Weather*, 3, S03001, <https://doi.org/10.1029/2004SW000104>.

Dungey, J. W. (1961). Interplanetary magnetic field and the auroral zones. *Physical Review Letters*, 6(2), 47–48. <https://doi.org/10.1103/PhysRevLett.6.47>.

Ebihara, Y., & Ejiri, M. (2000). Simulation study on fundamental properties of the storm-time ring current. *Journal of Geophysical Research*, 105(A7), 15,843–15,859. <https://doi.org/10.1029/1999JA900493>.

Ebihara, Y., & Miyoshi, Y. (2011). Dynamic inner magnetosphere: A tutorial and recent advance. In W. Liu, & M. Fujimoto (Eds.), *The dynamic magnetosphere* (pp. 145–187). *Springer*. https://doi.org/10.1007/978-94-007-0501-2_9.

Ebihara, Y., Ejiri, M., Nilsson, H., Sandahl, I., Milillo, A., Grande, M., et al. (2002). Statistical distribution of the storm-time proton ring current: POLAR measurements. *Geophysical Research Letters*, 29(20), 1969. <https://doi.org/10.1029/2002GL015430>.

Ebihara, Y., Yamada, M., Watanabe, S., & Ejiri, M. (2006). Fate of outflowing suprathermal oxygen ions that originate in the polar ionosphere. *Journal of Geophysical Research*, 111, A04219. <https://doi.org/10.1029/2005JA011403>.

Echer, E., Tsurutani, B. T., & Gonzalez, W. D. (2013). Interplanetary origins of moderate ($-100 \text{ nT} < \text{Dst} \leq -50 \text{ nT}$) geomagnetic storms during solar cycle 23 (1996–2008). *Journal of Geophysical Research: Space Physics*, 118, 385–392. <https://doi.org/10.1029/2012JA018086>.

Fok, M.-C., Kozyra, J. U., Nagy, A. F., & Cravens, T. E. (1991). Lifetime of ring current particles due to coulomb collisions in the plasmasphere. *Journal of Geophysical Research*, 96(A5), 7861–7867. <https://doi.org/10.1029/90JA02620>.

Fok, M.-C., Wolf, R. A., Spiro, R. W., & Moore, T. E. (2001). Comprehensive computational model of Earth's ring current. *Journal of Geophysical Research*, 106(A5), 8417–8424. <https://doi.org/10.1029/2000JA000235>.

Gkioulidou, M., Ukhorskiy, A. Y., Mitchell, D. G., & Lanzerotti, L. J. (2016). Storm time dynamics of ring current protons: Implications for the long-term energy budget in the inner

This article is protected by copyright. All rights reserved.

magnetosphere. *Geophysical Research Letters*, 43, 4736–4744.
<https://doi.org/10.1002/2016GL068013>.

Gonzalez, W. D., Joselyn, J. A., Kamide, Y., Kroehl, H. W., Rostoker, G., Tsurutani, B. T., & Vasyliunas, V. (1994). What is a geomagnetic storm. *Journal of Geophysical Research*, 99, 5771–5792. <https://doi.org/10.1029/93JA02867>.

Gonzalez, W.D., Tsurutani, B.T. & Clúa de Gonzalez, A.L. Interplanetary origin of geomagnetic storms. *Space Science Reviews* 88, 529–562 (1999).
<https://doi.org/10.1023/A:1005160129098>.

Gosling, J., Pizzo, V. Formation and Evolution of Corotating Interaction Regions and their Three-Dimensional Structure. *Space Science Reviews*, 89, 21–52 (1999).
<https://doi.org/10.1023/A:1005291711900>.

Greenspan, M. E., & Hamilton, D. C. (2002). Relative contributions of H⁺ and O⁺ to the ring current energy near magnetic storm maximum. *Journal of Geophysical Research*, 107(A4), 1043. <https://doi.org/10.1029/2001JA000155>.

Jahn, J. M., Goldstein, J., Reeves, G. D., Fernandes, P. A., Skoug, R. M., Larsen, B. A., & Spence, H. E. (2017). The warm plasma composition in the inner magnetosphere during 2012–2015. *Journal of Geophysical Research: Space Physics*, 122, 11018–11043. <https://doi.org/10.1002/2017JA024183>.

Jordanova, V. K., & Miyoshi, Y. S. (2005). Relativistic model of ring current and radiation belt ions and electrons: Initial results. *Geophysical Research Letters*, 32, L14104.
<https://doi.org/10.1029/2005GL023020>.

Jordanova, V. K., C. J. Farrugia, J. F. Fennell, and J. D. Scudder, Ground disturbances of the ring, magnetopause, and tail currents on the day the solar wind almost disappeared, *J. Geophys. Res.*, 106, 25529, 2001, <https://doi.org/10.1029/2000JA000251>.

Jordanova, V. K., C. J. Farrugia, L. Janoo, J. M. Quinn, R. B. Torbert, K. W. Ogilvie, R. P. Lepping, J. T. Steinberg, D. J. McComas, and R. D. Belian (1998), October 1995 magnetic cloud and accompanying storm activity: Ring current evolution, *J. Geophys. Res.*, 103, 79, <https://doi.org/10.1029/97JA02367>.

Jordanova, V. K., Kistler, L. M., Kozyra, J. U., Khazanov, G. V., & Nagy, A. F. (1996). Collisional losses of ring current ions. *Journal of Geophysical Research*, 101(A1), 111–126.
<https://doi.org/10.1029/95JA02000>.

Jordanova, V. K., L. M. Kistler, M. F. Thomsen, and C. G. Mouikis (2003), Effects of plasma sheet variability on the fast-initial ring current decay, *Geophys. Res. Lett.*, 30(6), 1311, <https://doi.org/10.1029/2002GL016576>.

This article is protected by copyright. All rights reserved.

Jordanova, V. K., Miyoshi, Y. S., Zaharia, S., Thomsen, M. F., Reeves, G. D., Evans, D. S., et al. (2006). Kinetic simulations of ring current evolution during the Geospace Environment Modeling challenge events. *Journal of Geophysical Research*, *111*, A11S10. <https://doi.org/10.1029/2006JA011644>.

Jordanova, V. K., Welling, D. T., Zaharia, S. G., Chen, L., & Thorne, R. M. (2012). Modeling ring current ion and electron dynamics and plasma instabilities during a high-speed stream driven storm. *Journal of Geophysical Research*, *117*, A00L08. <https://doi.org/10.1029/2011JA017433>.

Jordanova, V.K (2003), New Insights on Geomagnetic Storms from Model Simulations Using Multi-Spacecraft Data, *Space Science Reviews*, *107*, 157–165 <https://doi.org/10.1023/A:1025575807139>.

Kasahara, S., Yokota, S., Hori, T., Keika, K., Miyoshi, Y., & Shinohara, I. (2018a). The MEP-e instrument Level-2 3-D flux data of Exploration of energization and Radiation in Geospace (ERG) Arase satellite, Version v01_02. [Dataset]. ERG Science Center, Institute for Space-Earth Environmental Research, Nagoya University. <https://doi.org/10.34515/DATA.ERG-02000>.

Kasahara, S., Yokota, S., Hori, T., Keika, K., Miyoshi, Y., & Shinohara, I. (2018b). The MEP-e instrument Level-2 omni-directional flux data of Exploration of energization and Radiation in Geospace (ERG) Arase satellite, Version v01_02. [Dataset]. ERG Science Center, Institute for Space-Earth Environmental Research, Nagoya University. <https://doi.org/10.34515/DATA.ERG-02001>.

Kasahara, S., Yokota, S., Mitani, T., Asamura, K., Hirahara, M., Shibano, Y., & Takshima, T. (2018). Medium-energy particle experiments- electron analyzer (MEP-e) for the exploration of energization and radiation in geospace (ERG) mission. *Earth, Planets and Space*, *70*, 69. <https://doi.org/10.1186/s40623-018-0847-z>.

Katus, R. M., Liemohn, M. W., Ionides, E. L., Ilie, R., Welling, D., & Sarno-Smith, L. K. (2015). Statistical analysis of the geomagnetic response to different solar wind drivers and the dependence on storm intensity. *Journal of Geophysical Research: Space Physics*, *120*, 310–327. <https://doi.org/10.1002/2014JA020712>.

Kazama, Y., Wang, B. J., Wang, S. Y., Ho, P. T. P., Tam, S. W. Y., Chang, T. F., et al. (2017). Low-energy particle experiments-electron analyzer (LEPe) onboard the Arase spacecraft. *Earth, Planets and Space*, *69*, 165. <https://doi.org/10.1186/s40623-017-0748-6>.

Keika, K., Brandt, P. C., Nosé, M., & Mitchell, D. G. (2011). Evolution of ring current ion energy spectra during the storm recovery phase: Implication for dominant ion loss processes. *Journal of Geophysical Research*, *116*, A00J20. <https://doi.org/10.1029/2010JA015628>.

This article is protected by copyright. All rights reserved.

Keika, K., Kasahara, S., Yokota, S., Hoshino, M., Seki, K., Nosé, M., et al. (2018). Ion energies dominating energy density in the inner magnetosphere: Spatial distributions and composition, observed by Arase/MEP-i. *Geophysical Research Letters*, 45, 12153–12162. <https://doi.org/10.1029/2018GL080047>.

Keika, K., Kistler, L. M., & Brandt, P. C. (2013). Energization of O⁺ ions in the Earth's inner magnetosphere and the effects on ring current buildup: A review of previous observations and possible mechanisms. *Journal of Geophysical Research: Space Physics*, 118, 4441–4464. <https://doi.org/10.1002/jgra.50371>.

Keika, K., Nose, M., Brandt, P., Ohtani, S., Mitchell, D. G., & Roelof, E. C. (2006). Contribution of charge exchange loss to the storm time ring current decay: IMAGE/HENA observations. *Journal of Geophysical Research*, 111, A11S12. <https://doi.org/10.1029/2006JA011789>.

Keika, K., Nose, M., Ohtani, S.-I., Takahashi, K., Christon, S. P., & McEntire, R. W. (2005). Outflow of energetic ions from the magnetosphere and its contribution to the decay of the storm time ring current. *Journal of Geophysical Research*, 110, A09210. <https://doi.org/10.1029/2004JA010970>.

Kistler, L. M., Ipavich, F. M., Hamilton, D. C., Gloeckler, G., & Wilken, B. (1989). Energy spectra of the major ion species in the ring current during geomagnetic storms. *Journal of Geophysical Research*, 94(A4), 3579–3599. <https://doi.org/10.1029/JA094iA04p03579>.

Kistler, L. M., Mouikis, C. G., Spence, H. E., Menz, A. M., Skoug, R. M., Funsten, H. O., et al. (2016). The source of O⁺ in the storm time ring current. *Journal of Geophysical Research: Space Physics*, 121, 5333–5349. <https://doi.org/10.1002/2015JA022204>.

Klein, L. W., and L. F. Burlaga (1982), Interplanetary magnetic clouds at 1 AU, *J. Geophys. Res.*, 87, 613–624, <https://doi.org/10.1029/JA087iA02p00613>.

Kozyra, J. U., & Liemohn, M. W. (2003). Ring current energy input and decay. *Space Science Reviews*, 109(1–4), 105–131. <https://doi.org/10.1023/B:SPAC.0000007516.10433.ad>

Kozyra, J. U., Liemohn, M. W., Clauer, C. R., Ridley, A. J., Thomsen, M. F., Borovsky, J. E., et al. (2002). Multistep Dst development and ring current composition changes during the 4–6 June 1991 magnetic storm. *Journal of Geophysical Research*, 107(A8), 1224. <https://doi.org/10.1029/2001JA000023>.

Kumar, S., Miyoshi, Y., Jordanova, V. K., Engel, M., Asamura, K., Yokota, S., et al. (2021). Contribution of electron pressure to ring current and ground magnetic depression using RAM-SCB simulations and Arase observations during 7–8 November 2017 magnetic storm. *Journal*

of *Geophysical Research: Space Physics*, 126, e2021JA029109.
<https://doi.org/10.1029/2021JA029109>.

Kumar, S., Veenadhari, B., Chakrabarty, D., Tulasi Ram, S., Kikuchi, T., & Miyoshi, Y. (2020). Effects of IMF By on ring current asymmetry under southward IMF Bz conditions observed at ground magnetic stations: Case studies. *Journal of Geophysical Research: Space Physics*, 125, e2019JA027493. <https://doi.org/10.1029/2019JA027493>.

Li, H., Wang, C., & Kan, J. R. (2011). Contribution of the partial ring current to the SYM-H index during magnetic storms. *Journal of Geophysical Research*, 116, A11222. <https://doi.org/10.1029/2011JA016886>.

Liemohn, M. W., Kozyra, J. U., Clauer, C. R., & Ridley, A. J. (2001). Computational analysis of the near-Earth magnetospheric current system during two-phase decay storms. *Journal of Geophysical Research*, 106(A12), 29,531–29,542. <https://doi.org/10.1029/2001JA000045>.

Liemohn, M. W., Kozyra, J. U., Jordanova, V. K., Khazanov, G. V., Thomsen, M. F., & Cayton, T. E. (1999). Analysis of early phase ring current recovery mechanisms during geomagnetic storms. *Geophysical Research Letters*, 26(18), 2845–2848. <https://doi.org/10.1029/1999GL900611>.

McIlwain, C. E. (1961). Coordinates for mapping the distribution of magnetically trapped particles. *Journal of Geophysical Research*, 66 (11),3681–3691. <https://doi.org/10.1029/JZ066i011p03681>.

Menz, A. M., Kistler, L. M., Mouikis, C. G., Spence, H. E., Skoug, R. M., Funsten, H. O., et al. (2017). The role of convection in the build-up of the ring current pressure during the 17 March 2013 storm. *Journal of Geophysical Research: Space Physics*, 122, 475–492. <https://doi.org/10.1002/2016JA023358>.

Miyoshi, Y., Kataoka, R., (2005), Ring current ions and radiation belt electrons during geomagnetic storms driven by coronal mass ejections and corotating interaction regions. *Geophys. Res. Lett.* 32, L21105, <https://doi.org/10.1029/2005GL024590>.

Miyoshi, Y. S., Jordanova, V. K., Morioka, A., Thomsen, M. F., Reeves, G. D., Evans, D. S., & Green, J. C. (2006). Observations and modeling of energetic electron dynamics during the Oct. 2001 storm. *Journal of Geophysical Research*, 111, A11S02. <https://doi.org/10.1029/2005JA011351>.

Miyoshi, Y. S., & Kataoka, R. (2008). Flux enhancement of the outer radiation belt electrons after the arrival of stream interaction regions. *Journal of Geophysical Research*, 113, A03S09. <https://doi.org/10.1029/2007JA012506>.

Miyoshi, Y., and R. Kataoka (2011), Solar cycle variations of outer radiation belt and its relationship to solar wind structure dependences, *J. Atmos. Sol. Terr. Phys.*, 73(2011), 77–87, <https://doi.org/10.1016/j.jastp.2010.09.031>.

Miyoshi, Y. S., Kataoka, R., Kasahara, Y., Kumamoto, A., Nagai, T., & Thomsen, M. (2013). High-speed solar wind with southward interplanetary magnetic field causes relativistic electron flux enhancement of the outer radiation belt via enhanced condition of whistler waves. *Geophysical Research Letters*, 40, 4520–4525. <https://doi.org/10.1002/grl.50916>.

Miyoshi, Y. S., Shinohara, I., Takashima, T., Asamura, K., Higashio, N., Mitani, T., et al. (2018a). Geospace exploration project ERG. *Earth, Planets and Space*, 70, 101. <https://doi.org/10.1186/s40623-018-0862-0>.

Miyoshi, Y. S., Hori, T., Shoji, M., Teramoto, M., Chang, T. F., Segawa, T., et al. (2018b). The ERG science center. *Earth, Planets and Space*, 70(1), 1–11. <https://doi.org/10.1186/s40623-018-0867-8>.

Miyoshi, Y., I. Shinohara and C.-W. Jun (2018c), The Level-2 orbit data of Exploration of energization and Radiation in Geospace (ERG) Arase satellite, L2 v02, [Dataset], 10.34515/DATA.ERG-12000, [https://doi.org/DOI: 10.34515/DATA.ERG-12000](https://doi.org/DOI:10.34515/DATA.ERG-12000).

Mouikis, C. G., Bingham, S. T., Kistler, L. M., Farrugia, C. J., Spence, H. E., Reeves, G. D., et al. (2019). The storm-time ring current response to ICMEs and CIRs using Van Allen Probe Observations. *Journal of Geophysical Research: Space Physics*, 124, 9017–9039. <https://doi.org/10.1029/2019JA026695>.

Ni, B., Li, W., Thorne, R. M., Bortnik, J., Ma, Q., Chen, L., et al. (2014). Resonant scattering of energetic electrons by unusual low-frequency hiss. *Geophysical Research Letters*, 41, 1854–1861. <https://doi.org/10.1002/2014GL059389>.

Nose, M., Takahashi, K., Ohtani, S., Christon, S. P., & McEntire, R. W. (2005). Dynamics of ions of ionospheric origin during magnetic storms: Their acceleration mechanism and transport path to ring current. In T. I. Pulkkinen, N. A. Tsyganenko, & R. H. Friedel (Eds.), *The inner magnetosphere: Physics and modeling (Geophys. Monogr. Ser., Vol. 155, pp. 61–71)*. <https://doi.org/10.1029/155gm08>.

Sandhu, J. K., Rae, I. J., Freeman, M. P., Forsyth, C., Gkioulidou, M., Reeves, G. D., et al. (2018). Energization of the ring current by substorms. *Journal of Geophysical Research: Space Physics*, 123, 8131–8148. <https://doi.org/10.1029/2018JA025766>.

Sckopke, N (1966), A general relation between the energy of trapped particles and the disturbance field near the Earth, *J. Geophys. Res.*, 71, 3125. <https://doi.org/10.1029/JZ071i013p03125>.

This article is protected by copyright. All rights reserved.

Singer, S. F. (1957). A new model of magnetic storms and aurorae. *Eos, Transactions American Geophysical Union*, 38(2), 175-190. <https://doi.org/10.1029/TR038i002p00175>.

Smith, P. H., Bewtra, N. K., & Hoffman, R. A. (1981). Inference of the ring current ion composition by means of charge exchange decay. *Journal of Geophysical Research*, 86(A5), 3470. <https://doi.org/10.1029/JA086iA05p03470>.

Sugiura, M (1964), Hourly Values of Equatorial Dst for the IGY; *Pergamon Press: Oxford, UK*, pp. 7–45.

Sugiura, M., & Kamei, T. (1991). Equatorial Dst index 1957–1986, *IAGA Bull.*, 40, ISGI Pub., Office, Saint-Maur-des-Fosses, France.

Temporin, A., & Ebihara, Y. (2011). Energy-dependent evolution of ring current protons during magnetic storms. *Journal of Geophysical Research: Space Physics*, 116(A10), A10201. <https://doi.org/10.1029/2011ja016692>.

Tsurutani, B. T., Gonzalez, W. D., Gonzalez, A. L. C., Guarnieri, F. L., Gopalswamy, N., Grande, M., et al. (2006). Corotating solar wind streams and recurrent geomagnetic activity: A review. *Journal of Geophysical Research*, 111, A07S01. <https://doi.org/10.1029/2005JA011273>.

Tsyganenko, N. A., & Sitnov, M. I. (2005). Modeling the dynamics of the inner magnetosphere during strong geomagnetic storms. *Journal of Geophysical Research*, 110, A03208. <https://doi.org/10.1029/2004JA010798>.

Turner, N. E., Cramer, W. D., Earles, S. K., & Emery, B. A. (2009). Geoefficiency and energy partitioning in CIR-driven and CME-driven storms. *Journal of Atmospheric and Solar-Terrestrial Physics*, 71(10–11), 1023–1031. <https://doi.org/10.1016/j.jastp.2009.02.005>.

Wang, S.-Y., Kazama, Y., Jun, C.-W., Chang, T.-F., Hori, T., Miyoshi, Y., & Shinohara, I. (2018a). The LEPe instrument level-2 3-D flux data of Exploration of energization and Radiation in Geospace (ERG) Arase satellite, Version v02_02. [Dataset]. ERG Science Center, Institute for Space- Earth Environmental Research, Nagoya University. <https://doi.org/10.34515/DATA.ERG-04001>

Wang, S.-Y., Kazama, Y., Jun, C.-W., Chang, T.-F., Hori, T., Miyoshi, Y., & Shinohara, I. (2018b). The LEPe instrument level-2 omni-directional flux data of Exploration of energization and Radiation in Geospace (ERG) Arase satellite, Version v02_02. [Dataset]. ERG Science Center, Institute for Space-Earth Environmental Research, Nagoya University. <https://doi.org/10.34515/DATA.ERG-04002>.

Yokota, S., Kasahara, S., Hori, T., Keika, K., Miyoshi, Y., & Shinohara, I. (2018a). The MEP-i instrument Level-2 3-D flux data of Exploration of energization and Radiation in Geospace (ERG) Arase satellite, Version v01_03. [Dataset]. ERG Science Center, Institute for Space-Earth Environmental Research, Nagoya University. <https://doi.org/10.34515/DATA.ERG-03000>.

Yokota, S., Kasahara, S., Hori, T., Keika, K., Miyoshi, Y., & Shinohara, I. (2018b). The MEP-i instrument Level-2 omni-directional flux data of Exploration of energization and Radiation in Geospace (ERG) Arase satellite, Version v02_00. [Dataset]. ERG Science Center, Institute for Space-Earth Environmental Research, Nagoya University. <https://doi.org/10.34515/DATA.ERG-03001>.

Yokota, S., Kasahara, S., Mitani, T., Asamura, K., Hirahara, M., Takashima, T., et al. (2017). Medium-energy particle experiments—ion mass analyzer (MEP-i) onboard ERG (Arase). *Earth, Planets and Space*, 69(1), 172. <https://doi.org/10.1186/s40623-017-0754-8>.

Yue, C., Bortnik, J., Li, W., Ma, Q., Gkioulidou, M., Reeves, G. D., et al. (2018). The composition of plasma inside geostationary orbit based on Van Allen Probes observations. *Journal of Geophysical Research: Space Physics*, 123, 6478–6493. <https://doi.org/10.1029/2018JA025344>.

Yue, C., Zong, Q., Wang, Y., Vogiatzis, I. I., Pu, Z., Fu, S., & Shi, Q. (2011). Inner magnetosphere plasma characteristics in response to interplanetary shock impacts. *Journal of Geophysical Research*, 116, A11206. <https://doi.org/10.1029/2011JA016736>.

Zhang, Q. H., Dunlop, M. W., Lockwood, M., Holme, R., Kamide, Y., Baumjohann, W., et al. (2011). The distribution of the ring current: Cluster observations. *Annales Geophysicae*, 29(9), 1655–1662, <https://doi.org/10.5194/angeo-29-1655-2011>.

Zhao, H., Li, X., Baker, D. N., Claudepierre, S. G., Fennell, J. F., Blake, J. B., et al. (2016). Ring current electron dynamics during geomagnetic storms based on the Van Allen Probes measurements. *Journal of Geophysical Research: Space Physics*, 121, 3333–3346. <https://doi.org/10.1002/2016JA022358>.

Zhao, H., Li, X., Baker, D. N., Fennell, J. F., Blake, J. B., Larsen, B. A., et al. (2015). The evolution of ring current ion energy density and energy content during geomagnetic storms based on Van Allen Probes measurements. *Journal of Geophysical Research: Space Physics*, 120, 7493–7511. <https://doi.org/10.1002/2015JA021533>.

Cane, H. V., and I. G. Richardson (2003), Interplanetary coronal mass ejections in the near-Earth solar wind during 1996-2002, *J. Geophys. Res.*,108 (A4), 1156, <https://doi.org/10.1029/2002JA009817>

Borovsky, J. E., and M. H. Denton (2006), Differences between CME-driven storms and CIR-driven storms, *J. Geophys. Res.*, 111, A07S08, <https://doi.org/10.1029/2005JA011447>.

Miyoshi, Y., K. Sakaguchi, K. Shiokawa, D. Evans, J. Albert, M. Connors, and V. Jordanova (2008), Precipitation of radiation belt electrons by EMIC waves, observed from ground and space, *Geophys. Res. Lett.*, 35, L23101, <https://doi.org/10.1029/2008GL035727>.

Summers, D., Ni, B., & Meredith, N. P. (2007). Timescales for radiation belt electron acceleration and loss due to resonant wave-particle interactions: 2. Evaluation for VLF chorus, ELF hiss, and electromagnetic ion cyclotron waves. *Journal of Geophysical Research*, 112, A0427. <https://doi.org/10.1029/2006JA011993>.

Kozyra, J. U., Rasmussen, C. E., Miller, R. H., & Lyons, L. R. (1994). Interaction of ring current and radiation belt protons with ducted plasmaspheric hiss: 1. Diffusion coefficients and timescales. *Journal of Geophysical Research*, 99(A3), 4069–4084, <https://doi.org/10.1029/93JA01532>.

Young, S. L., Denton, R. E., Anderson, B. J., & Hudson, M. K. (2002). Empirical model for μ scattering caused by field line curvature in a realistic magnetosphere. *Journal of Geophysical Research*, 107(A6). <https://doi.org/10.1029/2000JA000294>.

Young, S. L., Denton, R. E., Anderson, B. J., & Hudson, M. K. (2008). Magnetic field line curvature induced pitch angle diffusion in the inner magnetosphere. *Journal of Geophysical Research*, 113, A03210. <https://doi.org/10.1029/2006JA012133>.

Yu, Y., Tian, X., & Jordanova, V. K. (2020). The effects of field line curvature (FLC) scattering on ring current dynamics and isotropic boundary. *Journal of Geophysical Research: Space Physics*, 125, e2020JA027830. <https://doi.org/10.1029/2020JA027830>.

Ebihara, Y., & Ejiri, M. (1998). Modeling of solar wind control of the ring current buildup: A case study of the magnetic storms in April 1997. *Geophysical Research Letters*, 25(20), 3751–3754. <https://doi.org/10.1029/1998GL900006>.

Liu, S., Chen, M. W., Roeder, J. L., Lyons, L. R., & Schulz, M. (2005). Relative contribution of electrons to the storm time total ring current energy content. *Geophysical Research Letters*, 32, L03110. <https://doi.org/10.1029/2004GL021672>.